Geophysical Journal International

Geophys. J. Int. (2020) **223,** 526–542
Advance Access publication 2020 June 17
GJI Seismology

doi: 10.1093/gji/ggaa300

Physics-based simulation of sequences with multiple main shocks in Central Italy

Rodolfo Console [1,2] Maura Murru,[1] Paola Vannoli,[1] Roberto Carluccio,[1] Matteo Taroni[1] and Giuseppe Falcone[1]

[1] *Istituto Nazionale di Geofisica e Vulcanologia, INGV, Rome, Italy. E-mail: maura.murru@ingv.it*
[2] *Center of Integrated Geomorphology for the Mediterranean Area, CGIAM, Potenza, Italy*

Accepted 2020 June 8. Received 2020 June 5; in original form 2019 September 13

SUMMARY

The application of a physics-based earthquake simulator to Central Italy allowed the compilation of a synthetic seismic catalogue spanning 100 000 yr, containing more than 300 000 $M \geq 4.0$ simulated earthquakes, without the limitations that real catalogues suffer in terms of completeness, homogeneity and time duration. The seismogenic model upon which we applied the simulator code was derived from version 3.2.1 of the Database of Individual Seismogenic Sources (DISS; http://diss.rm.ingv.it/diss/), selecting, and modifying where appropriate, all the fault systems that are recognized in the portion of Central Italy considered in this study, with a total of 54 faults. Besides tectonic stress loading and static stress transfer as in the previous versions, the physical model on which the latest version of our simulation algorithm is based also includes the Rate and State constitutive law that helps to reproduce Omori's law. One further improvement in our code was also the introduction of trapezoidal-shaped faults that perform better than known faults. The resulting synthetic seismic catalogue exhibits typical magnitude, space and time features which are comparable to those in real observations. These features include the total seismic moment rate, the earthquake magnitude distribution, and the short- and medium-term earthquake clustering. A typical aspect of the observed seismicity in Central Italy, as well as across the whole Italian landmass and elsewhere, is the occurrence of earthquake sequences characterized by multiple main shocks of similar magnitude. These sequences are different from the usual earthquake clusters and aftershock sequences, since they have at least two main shocks of similar magnitude. Therefore, special attention was devoted to verifying whether the simulated catalogue includes this notable aspect. For this purpose, we developed a computer code especially for this work to count the number of multiple events contained in a seismic catalogue under a quantitative definition. We found that the last version of the simulator code produces a slightly larger number of multiple events than the previous versions, but not as large as in the real catalogue. A possible reason for this drawback is the lack of components such as pore-pressure changes due to fluid-diffusion in the adopted physical model.

Key words: Numerical modelling; Earthquake interaction, forecasting and prediction; Seismicity and tectonics; Statistical seismology.

1 INTRODUCTION

1.1 Earthquake clustering and multiple events

It is widely recognized that earthquakes do not occur randomly according to a time-independent (Poissonian) model. Typical short-term features that have been observed and classified under various definitions (e.g. Utsu 1969) are: earthquake clustering, foreshock–main shock–aftershock sequences and swarms. Overall, the above typical features can be recognized as 'spatio-temporal clustering' (Field 2019).

Time-dependent behaviour and non-random occurrence of seismicity can be regarded as a promising way to achieve better operational earthquake forecasting. An example of a quantitative model of short-term clustering is popularly known as the Epidemic Type Aftershock Sequence (ETAS, Ogata 1998; Console & Murru 2001; Console *et al*. 2003, 2017a, and references therein). A new implementation of ETAS, along with the elastic rebound hypothesis, is

included in the 3rd Uniform California Earthquake Rupture Forecast (UCERF3) background model (Field *et al.* 2017).

Another quantitative model of non-random earthquake occurrence is the Every Earthquake Precursory According to Scale (EEPAS) one, for which Rhoades & Evison (2004, 2005, 2006) used a specific definition of swarm, recognized as a precursor of strong earthquakes. Usually, swarms are qualitatively defined as events where a local area experiences sequences of many earthquakes striking in a relatively short period. Characteristically, no single earthquake in the sequence is obviously identifiable as the main shock. According to the quantitative definition adopted by Evison & Rhoades (1993), swarms are seismic sequences constituted by at least three earthquakes whose magnitudes are linked to each other by empirical rules as follows:

$M \geq 3.3$, M_1–$M_3 \leq 0.7$, or M_1–$M_3 = 0.8$ and M_1–$M_4 \leq 0.9$, where M is the magnitude of any earthquake in the sequence and M_1 is the largest magnitude in the sequence, M_2 the second largest, and so on.

In this paper, we deal with a different, specific type of short- and intermediate-term earthquake clustering, that is the occurrence of two or more earthquakes of similar and largest magnitudes in a limited space and time window (often called 'doublets', 'multiplets' or 'multiple events'). In this paper, a 'multiple event' is intended as a group of two or more similarly large earthquakes, in a limited well-specified space–time window.

Initially, 'multiple events' was used to identify groups of earthquakes with nearly identical waveforms originating from the same location (Poupinet *et al.* 1984). A more modern definition is the one adopted in this study, that is that of a single sequence having two (or more) main shocks of similar magnitude, sometimes occurring within tens of seconds, sometimes separated by years (Beroza *et al.* 1995). The similarity of magnitude distinguishes multiple events from aftershock sequences, the magnitude of which is typically thought to be smaller than that of the parent shock by about 1.2 magnitude units (Bath's law; Vere-Jones 1969), and decrease in frequency according to the Omori's law.

Based on the distance between the epicentres of earthquakes temporally close to each other, Kagan & Jackson (1999) showed that about 20 per cent of very large earthquakes (magnitude above 7.5) are doublets, and that, in some cases, 37–75 per cent of earthquakes are multiplets.

Another study concerning doublets and multiplets from the Harvard CMT catalogue in the Fiji–Kermadec–Tonga region was published by Gibowicz & Lasocki (2005). These authors defined a doublet as a pair of earthquakes (i) with a magnitude difference of no more than 0.25 units, (ii) whose centroids are separated by no more than 40 km for events with magnitude from 5.0 to 5.4, 60 km for events with magnitude from 5.5 to 5.9, and 90 km for events with magnitude equal to or greater than 6.0 and (ii) whose difference in occurrence time is no longer than 200, 300 and 450 d, respectively.

The same kind of behaviour has been typically observed for the largest Italian earthquake sequences, such as the 1997 Appennino umbro-marchigiano, the 2002 Molise and the 2012 Emilia earthquake sequences (panel A, B and C in Fig. 1, respectively; Table 1). This is also the case of the three earthquakes having $M_w \geq 6.0$ occurred in Central Italy in 2016 over a period of 2 months and within about 30 km. From the examples in Fig. 1 we may infer that these doublets and multiplets did not occur on the same fault but on neighbouring seismogenic sources, which may or may not belong to the same fault system. As a matter of fact, the causative faults of the two Emilia 2012 main shocks belong to two different fault systems (see panel C in Fig. 1). Notice that the first large event triggers an even larger one that nucleates near the outer edges of the rupture zone. In the above-mentioned sequences numerous faults are involved, each of them responsible for a main shock, all very close in time and space. This occurrence can be found throughout all of Italy, from north to south, regardless of the kinematics (shown at the bottom of each panel).

1.2 Earthquake clustering in Italy

In the Catalogue of strong earthquakes in Italy and in the Mediterranean area (CFTI5Med) damaging events are documented since 461 BC (Guidoboni *et al.* 2018, 2019), but the seismic catalogue can be considered complete for $M_w \geq 6.0$ only for the last five centuries, during which no more than one large earthquake is reported for most individual faults (DISS Working Group 2018).

In our study we examine the presence of multiple events in real and simulated catalogues, adopting an empirical definition of such events similar, but not identical, to the definition of swarms introduced by Evison & Rhoades (1993). The definition of 'multiple events' quite varies from one author to another; our definition of multiple events is thus distinguished by magnitude criteria. We established a lower magnitude threshold of 5.5 for the first earthquake of the multiple sequence (M_A). This threshold is considered as the minimum earthquake magnitude that may produce damage to the man-made environment, and provides significant evidence of active crustal deformation (Basili *et al.* 2008) This is in agreement with the lower magnitude limit of earthquakes considered in the Database of Individual Seismogenic Sources (DISS). Our multiple events are also characterized by at least two main shocks, whose magnitudes M_A and M_B are within 0.5 units of each other, therefore $|M_A–M_B| \leq 0.5$. Notice that sequences with similarly large main shocks are common in Italy (Fig. 1 and Table 1) and have been observed also in other seismic regions of the world (e.g. Evison & Rhoades 1993; Beroza *et al.* 1995; Kagan & Jackson 1999; Gibowicz & Lasocki 2005).

1.3 Earthquake simulators as a tool for understanding the seismogenic process

In the last decade, thanks to the ever-increasing computing power, many earthquake simulators were developed. They generate synthetic earthquake catalogues spanning thousands of years or longer. Earthquake simulators differ in the methodology and the geometry of the patch used in the topologic definition of fault complexities. In fact, there are simulators that are essentially based on the fit of the Gutenberg–Richter distribution (Parsons & Geist 2009) up to those that incorporate stress interaction between faults (*Virtual Quake*, Rundle *et al.* 2006; Sachs *et al.* 2012; *ALLCAL*, Ward 2012), adding the Rate & State dependent fault constitutive properties for the sliding strength of faults (*RSQSim*, Dieterich & Richards-Dinger 2010; Richards-Dinger & Dieterich 2012), or using the viscoelastic approach (Pollitz 2012). The evolution of the geometry patch, from square to triangle, is useful to change the modelling of the fault system from planar to curved surfaces (Barall & Tullis 2015). A recent paper by Field (2019) supports the usefulness of physics-based earthquake simulators for improving overall testing procedures of earthquake forecasting.

From the view point of the inter-event time distribution, *RSQSim* (Dieterich & Richards-Dinger 2010; Richards-Dinger & Dieterich 2012) is generally considered the only simulator that, following

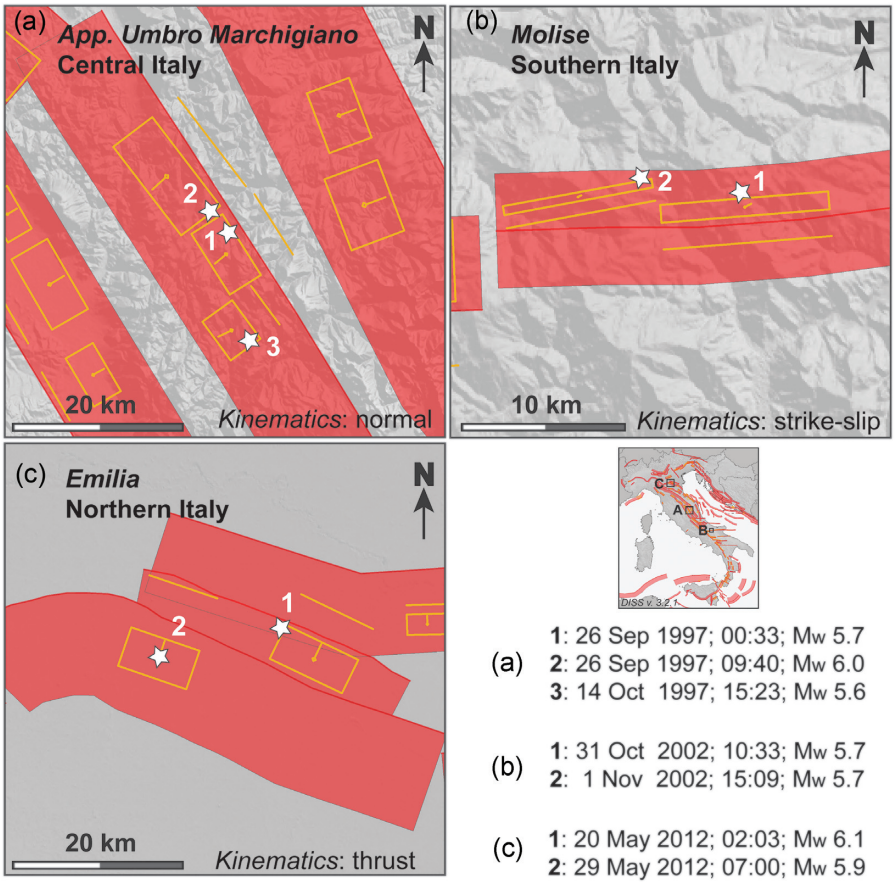

Figure 1. Three sequences consisting of two or three earthquakes with similar maximum magnitudes that occurred in Italy in 1997 (panel a), 2002 (panel b) and 2012 (panel c). The yellow boxes and the red ribbons are the projections onto the ground surface of the individual and composite seismogenic sources of Database of Individual Seismogenic Sources, DISS (DISS Working Group 2018), respectively. In particular, the yellow boxes are 3-D rectangular rupture planes that best approximate the observed earthquake ruptures in 1997 (panel a), 2002 (panel b), and 2012 (panel c). The epicentres of the sequence main shocks are shown by white stars, and are labeled with an ID, date, UTC time of occurrence and magnitude. Note also that in panel (a) and (b) the causative faults (yellow boxes) belong to the same fault system (red ribbon), while in case C they belong to two parallel fault systems.

Table 1. Summary of the 14 largest Italian earthquake sequences with at least one event of $M_w \geq 6.0$ of the past 90 yr (1928–2018; data from CPTI15). Ten of these 14 sequences were multiple events, that is they were characterized by at least two large earthquakes whose magnitudes are within 0.5 units of each other (updated and modified from Vannoli *et al.* 2015a). The 'Date' column indicates the date of the first event of the sequence. The 'Multiple' column defines whether the sequence can be defined as a multiple event; the value can be: Y (yes), N (no). The last column 'Time interval' reports the time span between the first and the last large events of the sequence, and ranges from seconds to several months. N A^{-1} means that the 'Time interval' estimate is not applicable to a single event. Notice how multiple events are common over the whole Italian territory, and affect compressional, extensional and strike-slip environments. The sequences of 1997 and 2012 are shown in Fig. 1.

Date	Epicentral area	M_w	Kinematics	Multiple	Time interval
27 March 1928	*Carnia*	6.0	Thrust	Y	1 d
23 July 1930	*Irpinia*	6.7	Normal	N	N/A
18 October 1936	*Alpago Cansiglio*	6.1	Thrust	N	N/A
21 August 1962	*Irpinia*	6.1	Normal/Strike-slip	Y	35 min
19 July 1963	*Mar Ligure*	6.0	Thrust	Y	1 min
14 January 1968	*Valle del Belice*	6.5	Thrust/Strike-slip	Y	Days
6 May 1976	*Friuli*	6.4	Thrust	Y	Months
15 April 1978	*Golfo di Patti*	6.0	Strike-slip	N	N/A
23 November 1980	*Irpinia-Basilicata*	6.7	Normal	Y	40 s
5 May 1990	*Potentino*	6.0	Strike-slip	Y	1 yr
26 September 1997	*Appennino umbro-marchigiano*	6.0	Normal	Y	18 d
6 April 2009	*L'Aquila*	6.2	Normal	N	N/A
20 May 2012	*Emilia*	6.1	Thrust	Y	9 d
24 Aug 2016	*Appennino centrale*	6.2	Normal	Y	2 months

a significant earthquake as well as aftershocks, shows the time-dependent increase in the conditional probability of nearby earthquakes (Tullis *et al.* 2012; Field 2015). Dieterich & Richards-Dinger (2010) explicitly mention the occasional presence of multiple events occurring as pairs, and more rarely as triplets, in their simulated catalogues. However, they found these features in an idealized fault system of about 400 km length and did not compare the frequency of these multiple events with real observations. We also note that Dieterich & Richards-Dinger (2010), unlike the method described later on in this study, do not apply any maximum distance criterion to their definition of multiple events; rather, they counted the pairs of simulated earthquakes occurring in their synthetic catalogue along the whole idealized fault system.

1.4 A new algorithm for detecting multiple events in real or simulated catalogues

In our study, we focus on the clustering features of synthetic catalogues produced by our new simulation algorithm and compare them with similar features observed in real catalogues, with particular regard to the occurrence of multiple events.

The present scientific literature still does not have any papers on simulators that compare the presence of multiple events within synthetic and real earthquake catalogues. For this purpose, we specifically developed an algorithm for the clustering analysis of multiple events in real and/or synthetic catalogues.

The procedure analyses a given seismic catalogue working on comparisons among time-ordered couples of events *A*-to-*B*, where event *A* chronologically precedes event *B*. For each couple, the simultaneous satisfaction of our criteria defining multiple events is checked. The multiple events identified are thus chains of 'successful' *A*-to-*B* links (please see Appendix B for further details about this new algorithm).

2 SEISMOGENIC MODEL OF CENTRAL ITALY

Historical and instrumental earthquake catalogues show that the seismicity of Central Italy concentrates along the main axis of the mountain chain and the buried thrust fronts of the Apennines (Table 2). In general, the mountainous domain exhibits larger and more frequent earthquakes than the piedmont and coastal areas do (Fig. 2). The 13 January 1915 *Marsica*, M_w 7.1, earthquake is to-date the largest one to have occurred since 1500 AD in the study area (ID 17 in Fig. 2 and Table 2; e.g. Vannoli *et al.* 2012), and is one of the strongest earthquakes reported in the Italian historical and instrumental catalogues.

The seismogenic model of the study area consists of normal, reverse, and strike-slip sources located between the mountain chain and the Adriatic Sea (Fig. 2). The reverse faults are the frontal thrusts which are located offshore near the Adriatic coast and are responsible for some earthquakes in the region (see Vannoli *et al.* 2015b). The strike-slip faults are relatively deep (10–20 km depth range) E–W trending shear zones that affect the Apulian foreland beneath the Apennines thrust belt (e.g. Kastelic *et al.* 2013). The normal faults straddle the crest of the Apennines and include those responsible for the 1915 *Marsica* earthquake and for the 2016–2017 central Italy sequence (IDs 22a, 22b, 22c in Table 2). The latter sequence includes three main shocks which are similar in magnitude (6.2, 6.1 and 6.6 from Rovida *et al.* 2019) interspersed by smaller aftershocks—all within a very close spatial range. Therefore, the 2016–2017 sequence can be defined as a multiple event, including two large events whose magnitude differs by a maximum of 0.4 units within 30 km. Consequently, this central Italy sequence is rather different from those made up of a single large earthquake followed by aftershocks of decreasing frequency.

The Parametric Catalogue of the Italian Earthquakes (CPTI15; Rovida *et al.* 2019) reports 23 strong events in our study area with magnitudes that span from 5.95 to 7.08, from 1500 AD to 2014 (Table 2). Note that these two decimal digits by which M_w are reported in Table 2 do not represent an accuracy of 0.01 units but simply result of a conversion from other magnitude scales adopted in the compilation of CPTI15. From 2014 to the date of writing (2019) three earthquakes having $M_w \geq 6.0$ occurred in the study region (Bollettino Sismico Italiano; http://cnt.rm.ingv.it/bsi. As a matter of fact, the time elapsed between successive earthquakes on a particular Seismogenic Fault (SF) in the Italian landmass is thought to be near one or more millennia, and therefore the probability of an occurrence in the period covered by historical records ranges from low to very low (e.g. Valensise & Pantosti 2001).

Earthquake sequences characterized by multiple, similarly large main shocks are rather common over the whole Italian territory (Tables 1 and 2, respectively), as well as globally (Evison & Rhoades 1993; Beroza *et al.* 1995; Kagan & Jackson 1999; Gibowicz & Lasocki 2005). Ten out of the fourteen largest Italian sequences ($M_w \geq 6.0$) of the past 90 yr (CPTI15; Rovida *et al.* 2019) were multiple events, that is they were characterized by at least two main shocks whose magnitude are within 0.5 units of each other. The time interval between the first and the last main shocks of the sequence ranges from a few seconds to a few years (Table 1).

In our study area we analyse a much longer time interval, from 1500 AD onwards for events with $M_w \geq 6.0$ (Table 2). An earthquake sequence occurring, for example during the Renaissance, and consisting of multiple events very close in time and space to each other may show in historical catalogues under a single main shock, due to the lack of information from historical sources. Therefore, in the pre-instrumental period (before 1895) one cannot rule out that a seismic sequence has been characterized by multiple events (shown in the last column of Table 2 with N A^{-1}). In summary, the Italian territory is expected to repeatedly experience sequences with multiple main shocks, such as the 14 January and 2 February 1703 *Valnerina* and *Aquilano* events (magnitude 6.9 and 6.7, respectively; IDs 7a and 7b in Table 2). In fact, the majority of the strongest crustal earthquakes of the entire Italian seismic history, both historical and instrumental, exhibit this behaviour (Tables 1 and 2).

Static stress transfer was invoked as the major cause for the spatial-temporal clustering of large earthquakes within a small fraction of their estimated recurrence intervals (e.g. King & Cocco 2001). In addition to stress transfer among adjacent faults, their occurrence is likely related to the structural complexity throughout the Italian landmass, which causes active fault systems to coexist with numerous pre-existing transverse structures. On the one hand, a rupture that may occur in a single large earthquake may be effectively controlled by these transverse structures, by limiting the length of the fault and, subsequently, the resulting magnitude of the earthquake. However, on the other hand, they make the triggering of adjacent faults more likely. The change of the dominant stress field (both syn- and post-orogenic) through time and its overprint onto the fault network, both inherited and newly formed, are responsible for the observed intense fragmentation of the extensional and compressional fault systems (e.g. Anderson & Jackson 1987; Vannoli *et al.* 2015a; Buttinelli *et al.* 2018). The resulting fault

Table 2. Parameters of the 34 largest ($M_w \geq 6$) earthquakes that occurred in the study region since 1500 AD. Data from CPTI15 (Rovida *et al.* 2019) and Bollettino Sismico Italiano (for the last earthquake sequence of Central Italy in 2016–2017; M_w from Gasperini *et al.* 2013). The last column indicates whether there could be at least two nearby events in space and time (Gardner & Knopoff 1974) and in M_w (within 0.4 units of each other). Note that at least 22 out of 34 earthquakes belong to 10 multiple sequences. Y: yes, N: no, N/A: not applicable (if the historical catalogues do not contain enough information to recognize or to rule out the presence of a multiple event). M_e: Equivalent Magnitude, calculated on the basis of macroseismic data; ∗ from CFTI5Med (for five cases) (Guidoboni *et al.* 2019); ∗∗ from Monachesi *et al.* 2016 (only for ID 15a).

ID	Date	Time hh mm ss	Epicentral area	Lat (°)	Lon (°)	M_w	Multiple
1	13 Jun 1542	02 15 –	*Mugello*	44.006	11.385	6.02	N/A
2	10 Sep 1584	20 30 –	*Appennino forlivese*	43.862	11.992	5.97	N/A
3	6 Nov 1599	01 25 –	*Valnerina*	42.724	13.021	6.07	N/A
4a	8 Oct 1639	– – –	*Monti della Laga*	42.639∗	13.269∗	6.21 (M_e 6.1∗)	Y∗
4b	15 Oct 1639	00 30 –	*Monti della Laga*	42.652∗	13.247∗	- (M_e 6.2∗)	
5	24 Jul 1654	00 25 –	*Sorano*	41.635	13.683	6.33	N/A
6	22 Mar 1661	12 50 –	*Appennino forlivese*	44.021	11.898	6.05	N/A
7a	14 Jan 1703	18 18 – –	*Valnerina*	42.708	13.071	6.92	Y
7b	2 Feb 1703	11 05 –	*Aquilano*	42.434	13.292	6.67	
8	3 Nov 1706	13 – –	*Maiella*	42.076	14.08	6.84	N/A
9a	12 May 1730	05 – –	*Valnerina*	42.753	13.12	6.04	Y∗
9b∗	12 May 1730	13 45 –	*Valnerina*	42.753	13.12	N/A	
10	24 Apr 1741	09 20 –	*Fabrianese*	43.425	13.005	6.17	N/A
11a∗	26 Jan 1747	– – –	*Appennino umbro-marchigiano*	N/A	N/A	N/A	Y∗
11b	17 Apr 1747	16 20 –∗	*Appennino umbro-marchigiano*	43.204	12.769	6.05	
12	27 Jul 1751	– – –	*Appennino umbro-marchigiano*	43.225	12.739	6.38	N/A
13a	19 Oct 1768	23 – –	*Appennino forlivese*	43.943	11.904	5.99	Y∗
13b∗	19 Oct 1768	23 – – (a few minutes later 13a)	*Appennino forlivese*	N/A	N/A	N/A	
14	3 Jun 1781		*Cagliese*	43.596	12.512	6.51	N/A
15a	28 Jul 1799	22 05 –	*Appennino marchigiano*	43.193	13.151	6.18	Y∗∗
15b	28 Jul 1799	– – –	*Appennino marchigiano*	N/A	N/A	N/A	
16a	13 Jan 1832	13 – –	*Valle Umbra*	42.98	12.605	6.43	Y∗
16b∗	13 Mar 1832	03 30 –	*Valle Umbra*	N/A	N/A	N/A	
17	13 Jan 1915	06 52 43	*Marsica*	42.014	13.53	7.08	N
18	26 Apr 1917	09 35 59	*Alta Valtiberina*	43.467	12.129	5.99	N
19a	10 Nov 1918	15 12 28	*Appennino forlivese*	43.917	11.933	5.96	Y
19b	29 Jun 1919	15 06 13	*Mugello*	43.957	11.482	6.38	
20a	26 Sep 1997	00 33 12	*Appennino umbro-marchigiano*	43.022	12.891	5.66	Y
20b	26 Sep 1997	09 40 26	*Appennino umbro-marchigiano*	43.014	12.853	5.97	
20c	14 Oct 1997	15 23 10	*Valnerina*	42.898	12.898	5.62	
21	6 Apr 2009	01 32 40	*Aquilano*	42.309	13.510	6.29	N
22a	24 Aug 2016	01 36 32	*Appennino centrale*	42.698	13.234	6.19	Y
22b	26 Oct 2016	19 18 07	*Appennino centrale*	42.909	13.129	6.06	
22c	30 Oct 2016	06 40 17	*Appennino centrale*	42.832	13.111	6.59	

network may thus play a further, important role by channeling fluid flow and controlling the timing of subsequent failure throughout the sequence. Finally, fluid overpressure appears to play a role in the partial remobilization of unbroken segments of the seismogenic fault systems (e.g. Buttinelli *et al.* 2018; Walters *et al.* 2018).

The seismogenic model upon which we applied the simulator code was derived from DISS, version 3.2.1 (Basili *et al.* 2008; DISS Working Group 2018; http://diss.rm.ingv.it/diss/). One of the core characteristics of DISS is the *Composite Seismogenic Sources* (CSS), fully parametrized crustal faults, thought to be capable of producing $M \geq 5.5$ earthquakes. The CSSs are based on regional surface and subsurface geological data developed well beyond the identification of active faults. We converted the CSSs identified in central Italy into 54 Seismogenic Fault systems (SFs), new sources with a trapezoidal shape, instead of the conventional rectangular one, specifically developed for this study (Fig. 2). The SFs are consistent with the parameters supplied for the CSSs. Each SF is thus characterized by: (1) the major axis of the source (strike); (2) the average dip angle; (3) the average value of the hanging-wall sense of motion (rake); (4) the depth intervals from sea level; (5) the maximum width obtained with average dip down to the maximum depth and (6) the slip rate of the respective CSS (Fig. 2). Table A1 in Appendix A lists the 54 SFs belonging to the study area, with their geometric and kinematics parameters.

3 ALGORITHM OF THE UPDATED SIMULATOR CODE

The algorithm of our simulator was initially introduced by Console *et al.* (2015), and successively modified by Console *et al.* 2017b, 2018a, b). The basic principles of the previous versions of the simulator were: (1) modelling the seismic sources by planar rectangular faults, each of which is discretized by square cells, the size of which is related to the minimum magnitude of the events in the output simulated catalogue; (2) tectonic stress loading of each fault according to observed slip rate; (3) nucleation of a new event when stress exceeds a given threshold strength on a cell; (4) coseismic stress release on each rupturing cell; (5) coseismic stress transfer from any rupturing cell to all other ones, according to the theory of elasticity; (6) expanding the rupture according to a heuristic rule that mimics

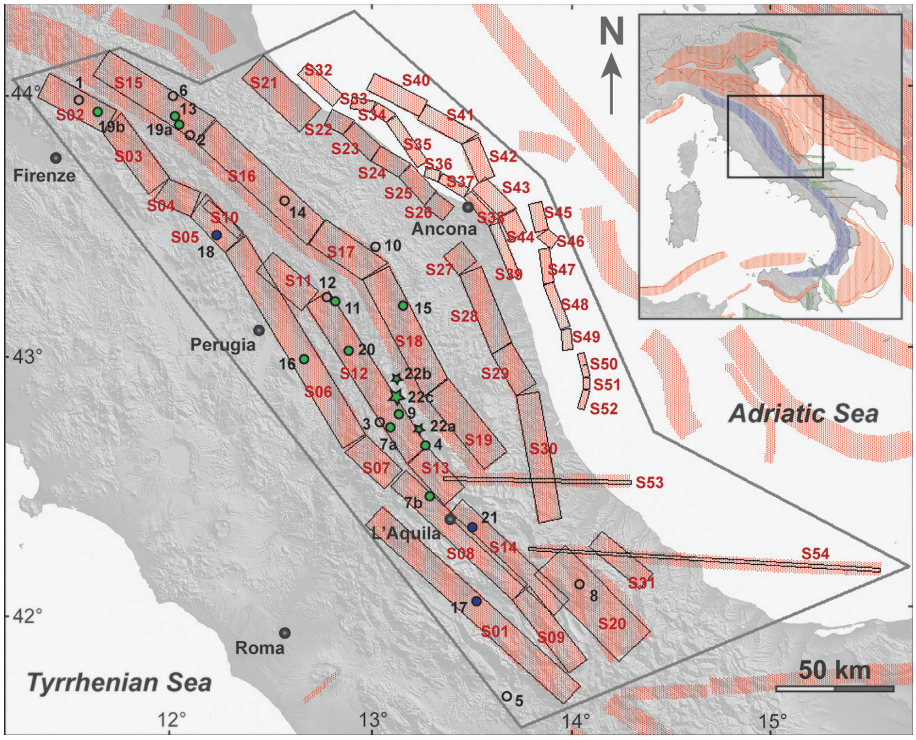

Figure 2. Seismotectonic setting of the study area showing the projections on the ground surface of the Seismogenic Fault system (SF) specifically developed for this study. The SFs are shown by polygons of four sides and are labelled in red with their IDs as in Table A1. The red ribbons are the projections on the ground surface of the CSSs from DISS 3.2.1 (DISS Working Group 2018). The epicentres of the CPTI15 earthquakes with $M_w \geq 6$ are shown by circles and are labelled with their IDs as in Table 2. The 3 events of the 2016–2017 sequence with $M_w \geq 6$ are shown by stars (Bollettino Sismico Italiano, http://cnt.rm.ingv.it/bsi). The earthquakes are shown in green if they belong to multiple events, in blue if they are single events (see text and Table 2), colourless if we do not know whether they are single or multiple earthquakes. The top right inset shows the areas with different faulting types (extensional in blue, compressional in red, and strike-slip in green).

a type of weakening mechanism; (7) allowing the rupture to jump from one source to a neighbouring one if the distance is shorter than a given threshold and (8) stopping the rupture when no other neighbouring cell meets the required stress threshold.

In this study, we apply a new version of the simulator, introducing new features with the aim of achieving a more realistic physical modelling of the seismic process and a better similarity between real and synthetic catalogues (Murru *et al.* 2018).

In the new version of the algorithm, a trapezoidal shape has improved the modelling of the geometry of the seismic source. It is noted that the old rectangular shapes, are special cases.

The rationale of this change is to allow a more accurate modelling of curved seismogenic structures, as described in the previous section, avoiding gaps between adjacent rectangular faults with different strikes.

Note that modelling the seismic sources using numerous faults of rectangular or trapezoidal shapes is just a convenient tool, simplifying the algorithm used in the physics-based simulator code, but in no way does it constrain a rupture to halt at the edges of such faults.

We then modified the algorithm of event nucleation, using the method described by Toda et al. (1998, 2005), based on the Rate & State constitutive law introduced by Dieterich (1994). Every cell of the fault system is characterized by the instantaneous value of its state variable γ. The expected rate r of failure of each cell in a population of identical cells is inversely proportional to γ as

$$r = \frac{\gamma_0 r_0}{\gamma}, \tag{1}$$

where γ_0 and r_0 are the unperturbed steady-state values of γ and r.

Every cell changes its stress status and consequently the values of γ and r according to its distance from the causative rupture. The coseismic Coulomb stress change ΔCFF on the receiving cell is computed by

$$\Delta CFF = \Delta\tau + \mu' \cdot \Delta\sigma_n \tag{2}$$

where $\Delta\tau$ and $\Delta\sigma_n$ are, respectively, the shear and the normal components of the stress change tensor inverted according to the focal mechanism of the receiver fault, and μ' is the effective coefficient of friction. Note that eq. (2) is calculated by adding the contribution of all cells ruptured in the causative event, with their respective coseismic slip.

According to the Rate & State model (Toda *et al.* 1998, 2005), the rate r' of failure after a time t from the causative event for the receiving cell is

$$r' = \frac{r_0}{\left[\frac{r_0}{r}\exp\left(\frac{\Delta CFF}{A\sigma}\right) - 1\right]\exp\left[-\frac{t}{t_a}\right] + 1}, \tag{3}$$

where r_0 is the background rate introduced in eq. (1), r is the rate of failure just before the causative event, $A\sigma$ is a constant parameter of the constitutive law and t_a is the characteristic decay time given by

$$t_a = \frac{A\sigma}{\dot{\tau}_r}, \tag{4}$$

where $\dot{\tau}_r$ is the stress rate (proportional to the slip rate) relative to the fault which the receiving cell belongs to. Here r_0 is the rate of events

of magnitude exceeding the threshold adopted in the simulation. It is obtained dividing the slip rate of each fault in the seismogenic model by the slip pertaining to an event of average magnitude, assuming a G–R distribution with $b = 1$, for events of magnitude exceeding the threshold.

After an event is stored in the output synthetic catalogue, the simulator makes use of eq. (3) to define the coordinates and occurrence time of a cell where the next event will nucleate, in the following iterative way. Let us suppose that the latest event occurs at the origin time t_0. The expected number N of new events in the time interval $t_0+\Delta t < t < t_0 + 1.5\Delta t$, can be obtained for all the cells of the fault system by integrating the occurrence rate of eq. (3) from Δt to $1.5\Delta t$ by, starting with a very small Δt time interval (e.g. one second). Here the integration is approximated by multiplying the occurrence rate at time $1.25\Delta t$ by $0.5\Delta t$. After a strong event, the cells with large positive ΔCFF will have high rates, and the cells with large negative ΔCFF will have low rates. The probability of at least one event occurring in the Δt time interval is given by 1-exp(-N) on the basis of a Poisson distribution. If a cell exists where the probability exceeds a random number uniformly distributed between 0 and 1, that cell is assigned as the nucleation point for a new event and its occurrence time is assigned a value randomly distributed between $t_0+\Delta t$ and $t_0 + 1.5\Delta t$, otherwise new probabilities are calculated, increasing Δt by a factor of 1.5 and compared with random numbers. If more than one cell fulfills the criterion of exceeding the random number, the cell with the largest probability is assumed as the nucleation cell. The process is repeated until the condition of exceedance for the probability in any of the cells is met and the rupture of a new event starts. According to eq. (3), after the rate change caused by an event, if no other perturbation happens, the rate r gradually returns to the background rate r_0.

By the application of this algorithm in the new version of the simulator, the nucleation point and occurrence time for events is randomly determined by a stochastic procedure, rather than by a deterministic rule. As it will be shown later, the synthetic catalogues obtained using this new algorithm were proven to contain realistic features of event clustering after strong events, not achieved by the previous versions.

In conclusion, the three free parameters that control the nucleation, propagation and stopping of a rupture in the simulator algorithm are:

(1) 'Strength Reduction' (*S–R*, Console *et al*. 2017b, 2018a, b), reducing the effective strength on the edges of an already nucleated rupture through a type of weakening mechanism; increasing this parameter favours the growth of ruptures, such as decreasing the *b*-value of the frequency–magnitude distribution; this parameter has a role similar to the η free parameter in the *Virtual Quake* simulator developed for California (Schultz *et al.* 2017);

(2) 'Aspect Ratio' (*A–R*; Console *et al*. 2015, 2017a, 2018a, b), restricting the propagation of a rupture beyond very long lengths; this parameter is relevant only if it is smaller than the ratio between the length and the width of the considered fault, and produces significant effects on the frequency–magnitude distribution only within a range of large magnitudes (see examples of the dependence of frequency–magnitude distribution on the choice of the value for the parameter A–R in fig. 5 of Console *et al.* 2015);

(3) $A\sigma$ of the Rate & State constitutive law (see eq. (3) above), having a strong effect on the probability of nucleation of events following the coseismic stress change due to previous events, and also inversely proportional to the characteristic decay time t_a through eq. (4).

It should be noted that none of the above-mentioned free parameters influence the average annual seismic moment rate, as this feature is totally controlled by the slip rate used in the algorithm through the fault system model. Few fluctuations are possible in short term simulated catalogues, due to either the rare occurrence or lack of very large earthquakes.

4 APPLICATION OF THE EARTHQUAKE SIMULATOR AND CLUSTERING ANALYSIS ALGORITHM TO CENTRAL ITALY

4.1 Search for the optimal value of the $A\sigma$ free parameter

The 54 sources shown in Fig. 2 and listed in Appendix A were discretized in cells of 0.75 km × 0.75 km. The smallest magnitude generated by a simulated earthquake rupturing a single cell is approximately 3.75 with a slip of 0.029 m and a seismic moment equal to 0.50E + 15 Nm, assuming a stress drop of 3.0 MPa.

Based on a previous study about the application of the simulator to the seismicity of the central Apennines (Console *et al.* 2018a) and on some preliminary trials with the present data set, we decided to consider the maximum values of the slip rates in our seismic source model, rather than the average (see Appendix A). This choice allows the compilation of synthetic catalogues whose total seismic moment rate is quite similar to that computed from the CPTI15 catalogue since 1650 (Rovida *et al.* 2019), as shown in Tables 4 and 5.

In this application, in order to allow a better comparison of the performances of the new version of the simulation algorithm with respect to the older one, we maintained the same values of $S–R = 0.2$ and $A–R = 2$ adopted by Console *et al.* (2018a) for the older version of the simulator. As to the $A\sigma$ free parameter, a wide range of values have been proposed, inferred from seismicity patterns observed in different earthquake sequences (Harris 1998). However, values in the range between 0.04 and 0.1 MPa seem to be most popular in the recent literature. For instance, Toda *et al.* (1998) proposed $A\sigma = 0.035 \pm 0.15$ MPa based on changes in seismicity rate following the 1995 Kobe earthquake. Catalli *et al.* (2008) determined $A\sigma$ from a maximum likelihood best fit of the observed seismicity for the area of Umbria-Marche in Central Italy, obtaining $A\sigma = 0.04$ MPa.

In this study, we carried out a series of seven tests allowing $A\sigma$ to range from 0.01 to 1.0 MPa.

The tests were all executed generating 10 000-yr-long synthetic catalogues. The preceding 2000 yr warm-up period, which was meant to lead the system to a stand-by status independent of the initial stress randomly assigned to every cell, was not included in this analysis.

Making use of the algorithm of clustering analysis mentioned in the Introduction, we obtained the total number of multiple events, each including at least two earthquakes, identified in the simulated catalogues. The arbitrary criteria adopted for this search were that a multiple event should start with a simulated earthquake of $M_A \geq 5.5$, followed by at least one earthquake in the M_A-0.5 $\leq M \leq M_A + 0.5$ magnitude range. This includes (i) a time delay according to the Gardner & Knopoff (1974) empirical rule applied to the first event of a couple, and (ii) a distance given to us by the radius, applying the same rule to the largest event of the same couple. This rule was chosen because it is the most used in PSHA (Probabilistic Seismic Hazard Analysis, van Stiphout *et al.* 2012); applying this type of declustering, the final declustered seismic catalogues usually follow a Poisson distribution. Telesca *et al.* (2016) compare

Table 3. Characteristics of the 10 000 yr long synthetic catalogues obtained with different values of $A\sigma$ and having fixed S-$R = 0.2$ and A-$R = 2$.

$A\sigma$ (MPa)	Number of events of $M \geq 5.0$	b-value ($M \geq 5.0$)	M_{mx}	Number of multiple events ($M_1 \geq 5.5$)
0.01	6060	1.284 ± 0.009	7.26	52
0.02	6746	1.259 ± 0.009	7.27	61
0.05	6686	1.229 ± 0.009	7.27	83
0.1	6471	1.222 ± 0.009	7.28	67
0.2	6115	1.162 ± 0.009	7.27	72
0.5	6728	1.177 ± 0.008	7.28	76
1.0	6553	1.198 ± 0.009	7.28	54

different declustering methods on the basis of time-correlation and space-clustering of the residual earthquake catalogue, concluding that the Gardner & Knopoff (1974) method seems to perform better in removing the time-correlation structures compared to other declustering methods.

The search was repeated for all pairs of simulated events. According to the clustering algorithm, the same simulated event was not allowed to be assigned to more than one multiple event. The results are listed in Table 3.

The number of multiple events does not exhibit a strong dependence on the value of the parameter $A\sigma$. However, the largest number is achieved by the choice of $A\sigma = 0.05$ MPa, with multiple events = 83. We thus adopted $A\sigma = 0.05$ MPa; regarding the further two free parameters of the simulator code, S–R and A–R, reported above, we have maintained the values obtained for the same area with the older version of the simulator algorithm (Console *et al.* 2018a), that is 0.2 and 2, respectively, for a comparison of the results between the two different versions. Both simulator codes were applied to the same Fault System, shown in Fig. 2 and listed in Appendix A (with the maximum values of the slip rate and the same values for S–R and A–R). These codes generated simulated catalogues for a period of 100 kyr, preceded by a warm-up period of 10 kyr not included in the output catalogues. We report the comparison results in Table 4. Shown in Fig. 3 is the real catalogue (left-hand panel) and the first 368 yr of the simulated catalogue (same temporal length of the real one, right-hand panel) along with the fault system: it is important to note that in the simulated catalogue epicentres are not allowed to fall outside the faults.

The b-values and their standard deviations were determined by the maximum likelihood method of Aki (1965) and the method introduced by Shi & Bolt (1982). Note the difference in the magnitude distribution between the two simulated catalogues. The new algorithm produced a significantly larger number of simulated events of magnitude $M \geq 5.0$ and consequently also a larger number of multiple events. The slight difference in the annual seismic moment release between the two catalogues can be justified by the fact that the total area of the trapezoidal faults is larger than that of the rectangular ones.

The last two rows of Table 4 report the number of multiple events with $M_1 \geq 5.5$ in the two synthetic catalogues (old and new version) and the number of multiple events with randomized occurrence times. In this table multiple events are defined in the same way as described above for the choice of the optimal value of the $A\sigma$ free parameter. Catalogue randomization is done by first generating a new time column for the catalogue table. This column contains unsorted values randomly extracted from a uniform distribution that spans the time length of the original catalogue. The new time values substitute the old ones and the randomization is thus achieved by time resorting the catalogue table rows.

It is pretty evident that the older version of the simulator does not produce a significant number of multiple events in excess of that pertaining to a completely random time distribution of the simulated events. Instead, the new version achieves a significant improvement in this respect.

4.2 Analysis of multiple events in the synthetic and real catalogs

For a comparison with real observations, we considered the CPTI15 catalogue since AD 1650, updated with the INGV instrumental catalogue (Bollettino Sismico Italiano, http://cnt.rm.ingv.it/bsi) until 30 April 2017, selected for our study area (shown by the black polygon in Fig. 2) with a minimum magnitude equal to 5.0. This magnitude, which is considered as the completeness magnitude of CPTI15 for this geographical area (Fig. 2) and the chosen time span (Rovida *et al.* 2019), is consistent with the search threshold for multiple events adopting the same criteria used for the synthetic catalogues. The results of the observed seismicity analysis are reported in Table 5.

The penultimate line of Table 5 shows 6 multiple events starting with an earthquake of $M_1 \geq 5.5$, contained exclusively in the CPTI15 catalogue. Out of these, four contain at least one earthquake with $M \geq 6.0$. They occurred in the sequences started on 14 January 1703, 10 November 1918, 26 September 1997 and 24 August 2016, respectively, and are also reported in Table 2. The other two multiple events, started on 22 November 1821 and 5 September 1950, contain only earthquakes with magnitude $5.5 < M < 6.0$, and are not reported in Table 2. We verified that, by using other catalogues and data, the number of sequences with multiple earthquakes in Italy can increase (see Table 2), but in this comparison we will only use the data of the Italian official parametric catalogue (CPTI15).

The last line of Table 5 reports the mean and the standard deviation of 30 randomized catalogues obtained from the updated CPTI15. These results show that the expected number of multiple events in a catalogue containing the same earthquakes out of CPTI15, although with completely random occurrence times, is lower than the observed multiple events (1.80 ± 1.40 against 6). The observed number of clusters, 6, is exactly 3σ times larger than 1.8, a value large enough to yield a robust statistical estimate (i.e. the observed number of clusters cannot be explained by a simple Poisson distribution of the events).

The comparison shown in Table 6 demonstrates that, even if the most recent version of the simulation algorithm achieves a significantly larger number of multiple events, it is clear that a predominance exists in the rate of multiple events in the observed seismicity of central Italy, with respect to that of the synthetic catalogue.

We should consider that the present version of the simulator algorithm does not include rheological constraints such as pore pressure changes and viscosity of the upper mantle, which are frequently mentioned as possible causes of slow stress variations and medium-term seismicity migration, as discussed in the following section.

5 DISCUSSION

5.1 Limitations of physical models

Our study is based on the application of an earthquake simulation algorithm based on relatively simple hypotheses. We are aware

Table 4. Features of the 100 000 yr synthetic catalogues obtained adopting S–$R = 0.2$ and A–$R = 2$ for the old and the new simulator one, at $A\sigma = 0.05$ MPa. The number of multiple events obtained by both codes, along with the number of multiple events in the respective randomized catalogues, are also reported.

	Old simulator code	New simulator code
Number of simulated events of $M \geq 4.0$	660 784	337 254
Maximum likelihood b-value ($M \geq 4.0$)	0.820 ± 0.0005	0.671 ± 0.0009
Number of simulated events of $M \geq 5.0$	52,773	71,679
Maximum likelihood b-value ($M \geq 5.0$)	1.182 ± 0.0032	1.209 ± 0.0026
Number of simulated events of $M \geq 6.0$	5315	5799
Maximum likelihood b-value ($M \geq 6.0$)	1.158 ± 0.0066	1.167 ± 0.0065
M_{max}	7.21	7.27
Annual seismic moment M_0 ($M \geq 4.0$)	5.23E + 17 Nm	5.70E + 17 Nm
Number of multiple events ($M_1 \geq 5.5$)	270	721
Number of multiple events ($M_1 \geq 5.5$) (Randomized catalogue)	272.6 ± 21.8	651.9 ± 26.4

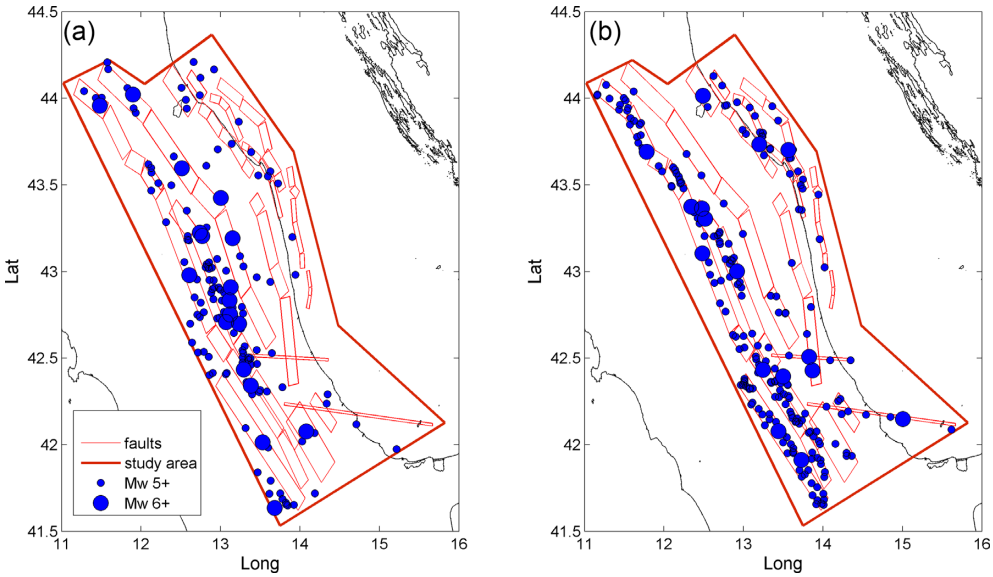

Figure 3. Epicentral maps of the real (left-hand panel) and simulated (right-hand panel) event catalogues; both maps refer to the same time period (368 yr); blue dots indicate the epicentres of the events; red lines indicate the fault areas and the external thick red polygon encloses the study area.

Table 5. Results of analysis of the updated CPTI15 catalogue (1650–2017, $M \geq 5.0$) including the number of multiple events for both the real and randomized occurrence times.

Number of earthquakes of $M \geq 5.0$	154
Maximum likelihood b-value ($M \geq 5.0$)	0.934 ± 0.050
Number of earthquakes of $M \geq 6.0$	18
Maximum likelihood b-value ($M \geq 6.0$)	1.092 ± 0.123
M_{max}	7.08
Annual seismic moment M_0 ($M \geq 5.0$)	5.44E + 17 Nm
Number of multiple events ($M_1 \geq 5.5$)	6
Number of multiple events ($M_1 \geq 5.5$) (Randomized catalogue)	1.80 ± 1.40

that models based on assumed physical interactions between specified faults can differ from actual earthquake processes. Needless to say, modeled events can occur only on prescribed faults. Unknown faults and differences in fault geometry could affect the results, and in fact many large earthquakes, for example in California (4 and 5 July 2019 Ridgecrest) and New Zealand (22 February 2011 Christchurch), have occurred outside of any previously known faults. Similarly, geologists in Italy have learnt important, and often surprising, lessons after each large earthquake. Here are some recent examples: (1–blind faulting) the 30 October–1 November 2002 Molise earthquakes occurred on hitherto unknown deep faults and highlighted an unexpected mode of earthquake release between the crest of the Apennines and the Adriatic coastline (Valensise *et al.* 2004); (2–hidden faulting) the causative fault of the 6 April 2009 L'Aquila earthquake had poorly expressed field evidence and was recognized before the 2009 event by only a few investigators (see Vannoli *et al.* 2012 and references therein); (3–negative inversion) the causative faults of the August–October 2016 central Italy sequence show the completely unexpected reactivation in extensional kinematics of old and well-known thrusts (e.g. Bonini *et al.* 2016, 2019).

As it is true of any earthquake simulation algorithm, we can say that our model relies on some hard to test assumptions. Likewise, not all results based on this kind of models can be tested in any detail against actual earthquakes. Nevertheless, models can be useful in developing hypotheses to explain earthquake observations, such as well-known statistical relationships such as the well-known statistical relationships of magnitude-frequency distribution, the temporal relationships of the Omori law and, in this paper, some qualities of earthquake clustering (see, e.g. Hainzl *et al.* 2003; Hainzl 2004;

Table 6. Comparison between the rate of multiple events contained in the simulated and observed seismicity.

	Synthetic catalogue old version (100 000 yr)	Synthetic catalogue new version (100 000 yr)	Real catalogue (368 yr)
Rate of events of $M \geq 5.5$ in 368 yr	46.7	63.3	67
Rate of multiple events with $M_1 \geq 5.5$ in 368 yr	1.08	2.65	6
Rate of multiple events with $M_1 \geq 5.5$ in 368 yr (randomized catalogue)	1.18	2.30	1.80 ± 1.40

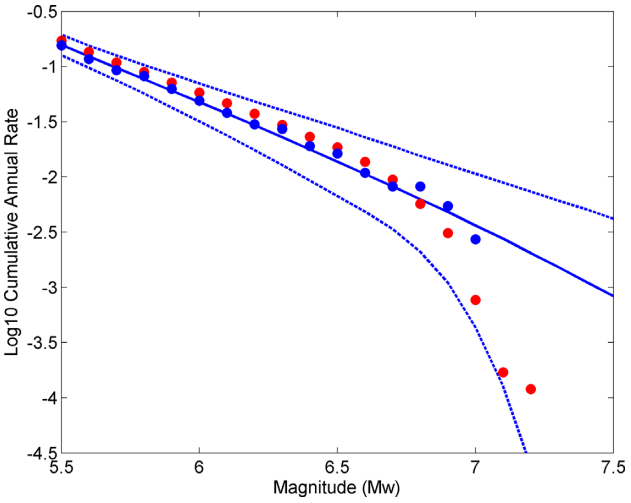

Figure 4. Magnitude-Frequency distributions of the simulated 100 000 yr catalogue (red dots) and the real DISS (1650–2017) catalogue (blue dots) for $M_w \geq 5.5$. The dashed blue lines show the 95 per cent confidence interval (relative to the epistemic uncertainty) of the model estimate from the observations, computed through a Monte Carlo approach, while the solid blue line shows the median.

Dieterich & Richards-Dinger 2010; Yikilmaz *et al.* 2011; Field 2019, among others). Moreover, in our study we have shown that the assumptions on the fault slip rate can be tested against real seismicity through the comparison of the expected and observed seismic moment rate.

5.2 Comparison of magnitude distribution and total seismic moment between real and simulated catalogs

In Fig. 4, we show the comparison of the cumulative magnitude-frequency distributions (MFDs) between the real (1650–2017, $M_w \geq 5.5$) and the synthetic catalogue obtained from the new version of the simulator, considering the maximum slip rate obtained from DISS. Such comparison shows a good similarity of the synthetic and real distributions, both in terms of total annual rate of events and *b*-value (close to 1). A slight exceedance of the annual rate in the 6.8–7.0 magnitude range can be justified by the limited period of observation (368 yr) and the uncertainty of the magnitude estimates for historical earthquakes. The maximum magnitude in the simulation, M_w 7.27, is smaller than the maximum possible magnitude that some seismogenic sources (e.g. S01 and S06) can accommodate according to the classical magnitude scaling relations. In our simulator algorithm the *A*–*R* parameter discourages the propagation of a rupture beyond a given number of times the fault width. In this work, we assumed $A–R = 2$, as adopted by Console *et al.* (2018a) for the older version of the simulator. To properly set this parameter we should compare the simulated catalogue against the palaeo-seismic one; in this work we only use the historical catalogue, so a detailed analysis of this parameter is left for future work.

The simulated MFD is within the 95 per cent confidence interval of the model estimation from the observations in all the magnitude range; to model the MFD we assume a tapered G–R distribution (Kagan 2002). We estimate the parameters using the Weichert 1980 method with a Monte Carlo Markov Chain approach to obtain the 95 per cent confidence interval of such estimation (Keller *et al.* 2014; Basili *et al.* 2019). The 95 per cent confidence interval is referred to the epistemic uncertainty, that is the uncertainty relative to the maximum likelihood estimation of the parameters.

While the magnitude distribution and temporal pattern of the simulated seismicity depends on the value assigned to each of the three free parameters used in the simulation algorithm, the total seismic moment released by the simulated earthquakes of the synthetic catalogue is controlled by the value of slip rate assumed for each fault. Table 5 shows that the annual seismic moment rate of the simulated real catalogues (obtained by summing moments for individual events) are similar. They are not identical because, in the long-term, the few largest events carry most of the moment rate.

In order to obtain a simulated catalogue with a total seismic rate similar to that of the updated CPTI15 catalogue, for our model we adopted the maximum slip rate reported in Table A1 of Appendix A (derived from DISS v. 3.2.1, 2018).

The comparison between the seismic moment rate of two simulated catalogues (obtained respectively from the previous and the enhanced versions of the simulator algorithm) and the real one is shown in Tables 4 and 5. The inadequacy of the mean slip rates to produce simulated catalogues with seismic moment rates similar to the observations could be explained by different circumstances such as: (1) overestimation of the magnitude estimates of the historical earthquakes; (2) underestimation of the slip rate of the fault model; (3) underestimation of the number and/or size of the SFs and (4) a non-constant trend of seismic moment release in time.

5.3 The role of fluid diffusion as a possible ingredient of the simulation algorithm

The results of the comparison between the observed and the simulated catalogues are reported in Table 6. They clearly show that the older version of the simulator code does not achieve a number of multiple events larger than that of a catalogue generated with random occurrence times. As far as multiple events are concerned, the new simulator code, incorporating the Rate & State friction model, exhibits substantial improvement, but still produces a smaller rate of multiple events with respect to the observed seismicity (Table 6). This can be ascribed to the lack of components such as visco-elastic and fluid migration in our current version of the simulator. Until now, the visco-elastic concept was only used in the *ViscoSim* earthquake simulator (Pollitz 2012). On the contrary, the influence of fluids migration has been so far left out of any published simulator algorithm (Field 2019).

The role of fluid diffusion in induced and natural seismicity has been given increasing attention in the last few decades. In their pioneering work, Nur & Booker (1972) argued that large shallow

earthquakes can induce changes in the fluid pore pressure that are comparable to stress drop on faults. The subsequent redistribution of pore pressure as a result of fluid flow slowly decreases the strength of rock and may result in delayed fracture providing an attractive mechanism for aftershocks.

Studying the seismicity induced in a hydraulic-fracturing experiment in Germany, Shapiro *et al.* (1997) developed a technique for estimating permeability using spatial-temporal distribution of the fluid-injection-induced seismic activity. They proposed a solution for the radius r of the expanding triggering front caused by a step-function point-source pore pressure in an isotropic homogeneous fluid saturated medium as:

$$r = \sqrt{4\pi Dt}, \tag{5}$$

where D is the diffusivity and t is time.

Yamashita (1998) modelled the spatio–temporal variation of rupture activity assuming fluid migration in a narrow, porous fault zone formed along a vertical strike-slip fault in a semi-infinite elastic medium. In particular the feature of earthquake swarms, characterized as a sequence of earthquakes in which there is no single predominant, principal event, is consistent with his modelling results if ruptures are forced to occur by fluid migration in a case where the fracture strength is relatively low and the initial tectonic stress is lower than the residual stress.

Later on, while studying the established connection between ascending magmatic fluids and seismicity, Parotidis *et al.* (2003) introduced a numerical model that successfully simulates the general spatial–temporal seismicity pattern of earthquake swarms in NW Bohemia (central Europe). In similar way Hainzl (2004), applied to the same earthquake swarms a model where earthquakes are triggered by fluid intrusion as well as by coseismic and post-seismic stress changes. The model is able to reproduce the main observations, such as the fractal temporal occurrence of earthquakes, embedded aftershock sequences, and a power-law increase of the average seismic moment release.

On the migration of seismic activity, including several main shocks in the same sequence, Antonioli *et al.* (2005) applied eq. (5) to model the seismicity pattern of the 1997 Umbria-Marche (central Italy) seismic sequence. Another application of eq. (5) was attempted by Pacchiani & Lyon-Caen (2010) to model the spatial–temporal evolution of the 2001 Agios Ioanis earthquake swarm (Corinth Rift, Greece) as the diffusion of a pore-pressure perturbation. They found an approximate speed of migration of 20 m d^{-1}, measured over 2 km and a period of 100 d.

More recently, several studies have been published where recent seismicity patterns characterized by migration of epicentral distribution were explained by the fluid flow model. Here we make a short review of some of these studies.

Rossi *et al.* (2016, 2017, 2018) analysed Global Navigation Satellite System (GNSS) observations in the northern Adria microplate to reveal non-periodic (transient) signals. They reported significant deviations from regional linear trends in the GNSS time series in an area about 150 km wide along the northern edge of the Adria microplate, focusing on a transient displacement with a duration of about 2.5 yr, recorded at 13 GNSS stations. An analysis of the arrival times of the transient signal revealed the source location and origin time. The disturbance appeared to have originated approximately 3.5 months prior to the M_w 5.2 earthquake that occurred near Bovec (Slovenia) in 2004. It was located 6.5 km NW of the main shock epicentre along the continuation of the recognized seismogenic Ravne fault and propagated with a mean velocity of 11 km yr^{-1}. For the sake of comparison, this velocity is much smaller than that inferred by Kagan & Knopoff (1976), who found a migration with a velocity between 300 and 2000 km yr^{-1} for epicentres of large aftershocks of $M \geq 7.0$ earthquakes worldwide.

Ross *et al.* (2017) analysed a vigorous aftershock sequence and post-seismic geodetic strain that occurred in the Yuha Desert following the 2010 M_w 7.2 El Mayor-Cucapah earthquake. The seismic and geodetic observations illuminate two distinct processes driving the aftershock sequence: early aftershocks were likely driven by afterslip; later aftershocks migrate according to eq. (5) and swarm-like behaviour, and were likely driven by fluid diffusion.

Mesimeri *et al.* (2016, 2017) carried out a detailed investigation on two earthquake swarms characterized by migration of epicentres. The first of these studies, devoted to the spatial-temporal evolution of the 2013 Aigion (Corinth Gulf, Greece) earthquake swarm, concluded that fluid flow cannot be unambiguously considered as the driving mechanism of the rupture process. The second one concluded that the high microseismic activity recorded near Florina (Greece) during July 2013–January 2014 can be interpreted as the consequence of CO_2 emission through faults, which may be used as path-ways in an area of coseismic Coulomb stress changes. Nespoli *et al.* (2018) introduced a model for the influence of fluids and coseismic pore-pressure changes on surface displacement and on the Coulomb failure function. They applied the model to the 2012 Emilia-Romagna (Italy) earthquakes, characterized by two main shocks of similar magnitude (6.1 and 6.0) separated only by 9 d. Their results show that the poro-elastic effect is small but not negligible and mostly confined in the near-field of the two main shocks.

Finally, as a recent step forward to modelling the interaction between fluid diffusion and seismicity, Michas & Vallianatos (2018) studied the diffusion properties of the 2001 Agios Ioannis earthquake swarm (Corinth Rift, Greece), which has been associated with fluid diffusion at depth. They mapped earthquake diffusion using a probabilistic approach and the continuous-time random walk theory (Helmstetter & Sornette 2002; Helmstetter *et al.* 2003).

When comparing results for different regions reported in the available literature, we find relevant differences in the velocity of fluid migration. This leads us to infer that modelling the fluid diffusion in an isotropic homogenously saturated medium, on which eq. (5) is based, is a largely oversimplified assumption, especially in a faulted medium. Recalling the wide range of time-differences between the earthquakes composing a multiple event reported in Tables 1 and 2, we may infer that the application of the type of model as that expressed by eq. (5) may pose a serious challenge for obtaining reliable results.

6 CONCLUSIONS

We applied a newly developed physics-based earthquake simulation algorithm to build a synthetic earthquake catalogue, the epicentres of which cover the whole seismic region of central Italy. The spatial distribution of the simulated seismicity is constrained by the geometrical parameters of the seismogenic model of central Italy derived from the DISS. Our algorithm allowed the simulation of a synthetic catalogue lasting 100 000 yr, and containing more than 300 000 simulated earthquakes with a minimum magnitude of 4.0.

In this study we focused on short- and medium-term seismicity patterns with particular reference to the occurrence of multiple events. A careful but somewhat qualitative analysis of the historical and instrumental catalogues (updated CPTI15 and CFTI5Med) of the $M_w \geq 6.0$ earthquakes reported in central Italy in the last five

centuries (Table 2) shows that at least 22 out of 34 earthquakes belong to 10 sequences with multiple events. During the time period, 1500–1703, only one sequence is reported in Table 2 as a multiple event. However, we cannot rule out that the five earthquakes that occurred prior to 1703 (1542, 1584, 1599, 1654 and 1661) can be considered multiple due to the possibility of missing historical information (N A^{-1} in Table 2).

This result is consistent with the analysis of the updated CPTI15 catalogue through an algorithm developed for this specific purpose, that is for multiple events starting with an earthquake of $M_w \geq 5.5$, as described in Section 5.2. Indeed, all four sequences with multiple events found since 1650 (1703, 1918, 1997 and 2016) by the specific code introduced in Section 1.4 are mentioned in Table 2, where the other five sequences with multiple events are inferred from information contained in other sources such as CFTI5Med (1730, 1747, 1768 and 1832) and Monachesi *et al.* 2016 (1799).

The same algorithm and criteria for the search of multiple events used for the analysis of the updated CPTI15 catalogue were also applied to two 100 000 yr simulated catalogues obtained respectively by our older and new simulation algorithm. It is the first time that a synthetic catalogue obtained by an earthquake simulator is compared with real observations from the point of view of generation of multiple events. This aspect of the Italian seismicity has always been disregarded despite its great importance in terms of seismic hazard. The results of the analysis achieved in this study show how the occurrence of multiplets in a real catalogue is not compatible with a purely random model. Therefore, such findings cannot be explained by a purely elastic model. The inclusion of the Dieterich's Rate & State model in our simulator algorithm, as it had already been shown by Dieterich & Richards-Dinger (2010), improved the results in this respect. However, our most recent version of the simulator still lacks the ability of producing multiple events as frequently as they can be observed in real catalogues.

We may conclude that, even if the aims of this study were limited to explore methodological aspects and potential capabilities of new-generation simulator algorithms, the initial results shown in this paper encourage further investigations about the capacity of simulators for a better comprehension of the seismic processes. it appears that an interesting ingredient for the improved modelling of earthquake clustering and earthquake sequences, such as multiple events by means of earthquake simulators, is earthquake triggering due to pore-pressure diffusion of underground fluids.

ACKNOWLEDGEMENTS

This work was funded by the Italian Project Ministry of Education, Research and University (MIUR) (https://www.iseki-food4.eu/work_packages/wp7/funding_agencies)

The authors are grateful to Margarita Segou, Editor, Eleftheria Papadimitriou, Reviewer, Louise Alexander, Assistant Editor, Umberto Fracassi and an anonymous Reviewer for their useful comments and suggestions that helped improving the quality of the manuscript.

REFERENCES

Aki, K., 1965. Maximum likelihood estimate of b in the formula log (N) = a-bM and its confidence limits, *Bull. Earthq. Res. Inst. Tokyo Univ.,* **43,** 237–239.

Anderson, H.A. & Jackson, J.A., 1987. Active tectonics of the Adriatic region, *Geophys. J. R. astr. Soc.,* **91,** 937–983.

Antonioli, A. Piccinini, D. Chiaraluce, L. & Cocco, M., 2005. Fluid flow and seismicity pattern: evidence from the 1997 Umbria-Marche (central Italy) seismic sequence, *Geophys. Res. Lett.,* **32,** L10311, doi:10.1029/2004GL022256.

Barall, M. & Tullis, T.E., 2015. The performance of triangular fault elements in earthquake simulators, *Seismol. Res. Lett.,* **87**(1), 164–170.

Basili, R. Valensise, G. Vannoli, P. Burrato, P. Fracassi, U. Mariano, S. Tiberti, M.M. & Boschi, E., 2008. The Database of Individual Seismogenic Sources (DISS), version 3: summarizing 20 years of research on Italy's earthquake geology, *Tectonophysics,* **453**(1-4), 20–53

Basili, R. *et al.*, 2019. *NEAMTHM18 Documentation: The Making of the TSUMAPS-NEAM Tsunami Hazard Model 2018,* Istituto Nazionale di Geofisica e Vulcanologia (INGV), doi:10.5281/zenodo.3406625.

Beroza, G.C. Cole, A.T. & Ellsworth, W.L., 1995. Stability of coda wave attenuation during the Loma Prieta, California, earthquake sequence, *J. Geol. Res.,* **100**(B3), 3977–3987.

Bonini, L. *et al.*, 2016. Imaging the tectonic framework of the 24 August 2016, Amatrice (central Italy) earthquake sequence: new roles for old players?, *Ann. Geophys.,* **59,** 5, doi: 10.4401/ag-7229.

Bonini, L. *et al.*, 2019. Testing different tectonic models for the source of the Mw 6.5, 30 October 2016, Norcia earthquake (central Italy): a youthful normal fault, or negative inversion of an old thrust?, *Tectonics,* **38,** doi:10.1029/2018TC005185.

Buttinelli, M. Pezzo, G. Valoroso, L. De Gori, P. & Chiarabba, C., 2018. Tectonics inversions, fault segmentation and triggering mechanisms in the Central Apennines normal fault system: insights from high-resolution velocity models, *Tectonics,* **37** (11), 4135–4149.

Catalli, F. Cocco, M. Console, R. & Chiaraluce, L., 2008. Modeling seismicity rate changes during the 1997 Umbria-Marche sequence (central Italy) through a rate-and state-dependent model, *J. geophys. Res.,* **113,** B11301, doi:10.1029/2007JB005356.

Console, R. & Murru, M., 2001. A simple and testable model for earthquake clustering, *J. geophys. Res.,* **106,** 8699–8711.

Console, R. Murru, M. & Lombardi, A.M., 2003. Refining earthquake clustering models, *J. geophys. Res.,* **108**(B10), 2468, doi:10.1029/2002JB002130.

Console, R. Carluccio, R. Papadimitriou, E. & Karakostas, V., 2015. Synthetic earthquake catalogs simulating seismic activity in the Corinth Gulf, Greece, fault system, *J. geophys. Res.,* **120**(1), 326–343.

Console, R. Murru, M. & Falcone, G., 2017a. *Earthquake Occurrence: Short- and Long-Term Models and their Validation. Mathematics and Statistics Series, Statistical Methods for Earthquakes Set,* Vol. **1,** ISTE - Wiley, pp. 135.

Console, R. Nardi, A. Carluccio, R. Murru, M. Falcone, G. & Parsons, T., 2017b. A physics-based earthquake simulator and its application to seismic hazard assessment in Calabria (Southern Italy) region, *Acta Geophys.,* **65,** 243–257.

Console, R. Vannoli, P. & Carluccio, R., 2018a. The seismicity of the Central Apennines (Italy) studied by means of a physics-based earthquake simulator, *Geophys. J. Int.,* **212,** 916–929.

Console, R. Chiappini, M. Minelli, L. Speranza, F. Carluccio, R. & Greco, M., 2018b. Seismic hazard in Southern Calabria (Italy) based on the analysis of a synthetic earthquake catalogue, *Acta Geophys.,* **66,** 931–943.

Dieterich, J., 1994. A constitutive law for rate of earthquake production and its application to earthquake clustering, *J. geophys. Res.,* **99**(B2), 2601–2618.

Dieterich, J.H. & Richards-Dinger, K.B., 2010. Earthquake recurrence in simulated fault systems, *Pure appl. Geophys.,* **167,** 1087–1104.

DISS Working Group, 2018. *Database of Individual Seismogenic Sources (DISS),* Version 3.2.1: a compilation of potential sources for earthquakes larger than M 5.5 in Italy and surrounding areas. http://diss.rm.ingv.it/diss/, Istituto Nazionale di Geofisica e Vulcanologia, doi:10.6092/INGV.IT-DISS3.2.1.

Evison, F.F. & Rhoades, D.A., 1993. The precursory earthquake swarm in New Zealand: hypothesis tests, *New Zeal. J. Geol. Geophys.,* **36,** 51–60.

Field, E.H., 2015. Computing elastic-rebound motivated earthquake probabilities in unsegmented fault models: a new methodology supported by physics-based simulators, *Bull. seism. Soc. Am.,* **105**(2A), 544–559.

Field, E.H. *et al.*, 2017. A spatiotemporal clustering model for the Third Uniform California Earthquake Rupture Forecast (UCERF3-ETAS): toward an operational earthquake forecast, *Bull. seism. Soc. Am.,* **107**(3), 1049–1081.

Field, E.H., 2019. How physics-based earthquake simulators might help improve earthquake forecasts, *Seismol. Res. Lett.,* **90** (2A), 467–472.

Gardner, J.K. & Knopoff, L., 1974. Is the sequence of earthquakes in Southern California, with aftershocks removed, Poissonian?, *Bull. seism. Soc. Am.,* **64**(5), 1363–1367.

Gasperini, P. Lolli, B. & Vannucci, G., 2013. Empirical calibration of local magnitude data sets versus moment magnitude in Italy, *Bull. seism. Soc. Am.,* **103,** 2227–2246.

Gibowitz, S.J. & Lasocki, S., 2005. Earthquake doublets and multiplets in the Fiji-Tonga-Kermadec region, *Acta Geophys. Pol.,* **53**(3), 239–274.

Guidoboni, E. Ferrari, G. Mariotti, D. Comastri, A. Tarabusi, G. Sgattoni, G. & Valensise, G., 2018. *CFTI5Med, Catalogo dei Forti Terremoti in Italia (461 a.C.-1997) e nell'area Mediterranea (760 a.C.-1500),* Istituto Nazionale di Geofisica e Vulcanologia (INGV), doi:10.6092/ingv.it-cfti5.

Guidoboni, E. *et al.*, 2019. CFTI5Med, the new release of the catalogue of strong earthquakes in Italy and in the Mediterranean area, *Sci. Data,* **6,** 80, doi:10.1038/s41597-019-0091-9.

Hainzl, S., 2004. Seismicity patterns of earthquake swarms due to fluid intrusion and stress triggering, *Geophys. J. Int.,* **159,** 1090–1096.

Hainzl, S. Zöller, G. & Scherbaum, F., 2003. Earthquake clusters resulting from delayed rupture propagation in finite fault segments. *J. geophys. Res.,* **108**(B1), ESE 4–1-ESE 4-10.

Harris, R.A., 1998. Introduction to special section: stress triggers, stress shadows, and implications for seismic hazard, *J. geophys. Res.,* **103**(24), 347–324, 358.

Helmstetter, A. & Sornette, D., 2002. Diffusion of epicenters of earthquake aftershocks, Omori's law, and generalized continuous-time random walk models, *Phys. Rev. E,* **66,** 061104.

Helmstetter, A. Oulliuon, G. & Sornette, D., 2003. Are aftershocks of large California earthquakes diffusing? *J. geophys. Res.,* **108,** ESE9–1-ESE9-24.

Kagan, Y. & Knopoff, L., 1976. Statistical search for non-random features of the seismicity of strong earthquakes, *Phys. Earth Planet Int.,* **12,** 291–318.

Kagan, Y.Y. & Jackson, D.D., 1999. Worldwide doublets of large shallow earthquake, *Bull. seism. Soc. Am.,* **89**(5), 1147–1155.

Kagan, Y.Y., 2002. Seismic moment distribution revisited: I. Statistical results, *Geophys. J. Int.,* **148**(3), 520–541.

Kastelic, V. Vannoli, P. Burrato, P. Fracassi, U. Tiberti, M.M. & Valensise, G., 2013. Seismogenic sources in the Adriatic Domain, *Mar. Petrol. Geol.,* **42,** 191–213.

Keller, M. Pasanisi, A. Marcilhac, M. Yalamas, T. Secanell, R. & Senfaute, G., 2014. A Bayesian methodology applied to the estimation of earthquake recurrence parameters for seismic hazard assessment, *Qual. Reliab. Eng. Int.,* **30**(7), 921–933.

King, G.C.P. & Cocco, M., 2001. Fault interaction by elastic stress changes: new clues from earthquake sequences, *Adv. Geophys.,* **44,** 1–38.

Maesano, F.E. Toscani, G. Burrato, P. Mirabella, F. D'Ambrogi, C. & Basili, R., 2013. Deriving thrust fault slip rates from geological modeling: examples from the Marche coastal and offshore contraction belt, Northern Apennines, Italy, *Mar. Petrol. Geol.,* **42,** 122–134.

Maesano, F.E. D'Ambrogi, C. Burrato, P. & Toscani, G., 2015. Slip-rates of blind thrusts in slow deforming areas: examples from the Po Plain (Italy), *Tectonophysics,* **643,** 8–25.

Mesimeri, M. Karakostas, V. Papadimitriou, E. Schaff, D. & Tsaklidis, G., 2016. Spatio-temporal properties and evolution of the 2013 Aigion earthquake swarm (Corinth Gulf, Greece), *J. Seismol.,* **20,** 595–614.

Mesimeri, M. Karakostas, V. Papadimitriou, E. Tsaklidis, G. & Tsapanos, T., 2017. Detailed microseismicity study in the area of Florina (Greece): evidence for fluid driven seismicity, *Tectonophysics,* **694,** 424–435.

Michas, G. & Vallianatos, F., 2018. Modelling earthquake diffusion as a continuous-time random walk with fractional kinetics: the case of the 2001 Agios Ioannis earthquake swarm (Corinth Rift), *Geophys. J. Int.,* **215,** 333–345.

Monachesi, G. Castelli, V. & Camassi, R., 2016. Aggiornamento delle conoscenze sul terremoto del 28 luglio 1799 nel sub-Appennino maceratese, *Quaderni di geofisica,* **138,** Istituto Nazionale di Geofisica e Vulcanologia.

Murru, M. Carluccio, R. Console, R. Falcone, G. Taroni, M. & Vannoli, P., 2018. Physics-based Simulator of Short-Term Seismicity: Application to the Central Apennines Region. AGU 2018 Fall Meeting, https://www.essoar.org/doi/abs/10.1002/essoar.10500076.1.

Nespoli, M. Belardinelli, M.E. Gualandi, A. Serpelloni, E. & Bonafede, M., 2018. Poroelasticity and fluid flow modeling for the 2012 Emilia-Romagna earthquakes: Hints from GPS and InSAR data, *Geofluids,* Article ID 4160570, doi:10.155/2018/41650570.

Nur, A. & Booker, J.R., 1972. Aftershocks caused by pore fluid flow?, *Science,* **175,** 885–887.

Ogata, Y., 1998. Space-time point-process models for earthquake occurrences, *Ann. Inst. Statist. Math.,* **50**(2), 379–402.

Pacchiani, F. & Lyon-Caen, H., 2010. Geometry and spatio-temporal evolution of the 2001 Agios Ioanis earthquake swarm (Corinth Rift, Greece), *Geophys. J. Int.,* **180,** 59–72.

Parotidis, M. Rothert, E. & Shapiro, S.A., 2003. Pore-pressure diffusion: A possible triggering mechanism for the earthquake swarms 2000 in Vogtland/NW-Bohemia, central Europe, *Geoph. Res. Lett.,* **30**(20), 2075, doi:10.1029/2003GL018110.

Parsons, T. & Geist, E.L., 2009. Is there basis for preferring characteristic earthquakes over Gutenberg-Richter distributions on individual faults in probabilistic earthquake forecasting?, *Bull. seism. Soc. Am.,* **99,** 2012–2019.

Pollitz, F.F., 2012. ViscoSim earthquake simulator, *Seismol. Res. Lett.,* **83,** 979–982.

Poupinet, G. Ellsworth, W.L. & Frechet, J., 1984. Monitoring velocity variations in the crust using earthquake doublets: an application to Calaveras Fault, California, *J. geophys. Res.,* **89,** 5719–5731.

Rhoades, D.A. & Evison, F.F, 2004. Long-range earthquake forecasting with every earthquake a precursor according to scale, *Pure appl. Geophys.,* **161,** 47–72.

Rhoades, D.A. & Evison, F.F., 2005. Test of the EEPAS forecasting model on the Japan earthquake catalogue. *Pure appl. Geophys.,* **162,** 1271–1290.

Rhoades, D.A. & Evison, F.F., 2006. The EEPAS forecasting model and the probability of moderate-to-large earthquakes in central Japan, *Tectonophysics,* **417,** 119–130.

Richards-Dinger, K. & Dieterich, J.H., 2012. RSQSim earthquake simulator, *Seismol. Res. Lett.,* **83**(6), 983–990.

Ross, Z.E. Rollins, C. Cochran, E.S. Hauksson, E. Avouac, J.-P. & Ben-Zion, Y., 2017. Aftershocks driven by afterslip and fluid pressure sweeping through a fault-fracture mesh, *Geophys. Res. Lett.,* **44,** 8260–8267.

Rossi, G. Zuliani, D. & Fabris, P., 2016. Long-term GNSS measurements through Northern Adria Microplate reveal fault-induced fluid mobilization, *Tectonophysics,* **690,** 142–159.

Rossi, G. Zuliani, D. & Fabris, P., 2017. Corrigendum to: 'Long-term GNSS measurements through Northern Adria Microplate reveal fault-induced fluid mobilization', *Tectonophysics,* **694,** 486–487.

Rossi, G. Fabris, P. & Zuliani, D., 2018. Overpressure and fluid diffusion causing non-hydrological transient GNSS displacements, *Pure appl. Geophys.,* **175,** 1869–1888.

Rovida, A. Locati, M. Camassi, R. Lolli, B. & Gasperini, P., 2019. *Catalogo Parametrico dei Terremoti Italiani (CPTI15),* versione 2.0. Istituto Nazionale di Geofisica e Vulcanologia (INGV). https://doi.org/10.13127/CPTI/CPTI15.2.

Rundle, P. Rundle, J. Tiampo, K. Donnellan, A. & Turcotte, D., 2006. Virtual California: fault model, frictional parameters, applications, in *Computational Earthquake Physics: Simulations, Analysis and Infrastructure, Part I. Pageoph Topical Volumes,* eds, Yin , X., Mora, P., Donnellan, A. & Matsu'ura, M., Birkhäuser.

Sachs, M.K. Heien, E.M. Turcotte, D.L. Yikilmaz, M.B. Rundle, J.B. & Kellogg, L.H., 2012. *Seismol. Res. Lett.,* **83**(6), 973–978.

Shapiro, S.A. Huenges, E. & Borm, G., 1997. Estimating the crust permeability from fluid-injection-induced seismic emission at the KTB site, *Geoph. J. Int.,* **131,** F15–F18.

Shi, Y. & Bolt, B.A., 1982. The standard error of the magnitude-frequency b-value, *Bull. seism. Soc. Am.,* **72,** 1677–1687.

Schultz, K.W. Yoder, M.R. Wilson, J.M. Heien, E.M. Sachs, M.K. Rundle, J.B. & Turcotte, D.L., 2017. Parametrizing phyisics-based earthquake simulations, *Pure appl. Geophys.,* **174,** 2269–2278.

Telesca, L. Lovallo, M. Golay, J. & Kanevski, M., 2016. Comparing seismicity declustering techniques by means of the joint use of Allan Factor and Morisita index. *Stoch. Environ. Res. Risk Assess,* **30**(1), 77.

Toda, S. Stein, R.S. Reasenberg, P.A. Dieterich, J.H. & Yoshida, A., 1998. Stress transferred by the 1995 M_w= 6.9 Kobe, Japan, shock: effect on aftershocks and future earthquake probabilities, *J. geophys. Res.,* **103**(B10), 24 543–24 565.

Toda, S. Stein, R. Richards-Dinger, K. & Bozkurt, S., 2005. Forecasting the evolution of seismicity in southern California: animations built on earthquake stress transfer, *J. geophys. Res.,* **110,** B05S16, doi:10.1029/2004JB003415.

Utsu, T., 1969. Aftershocks and earthquake statistics, *J. Facul. Sci., Hokkaido Univ., VII,* **3**(3), 129–195.

Tullis, T.E. *et al.*, 2012. A comparison among observations and earthquake simulator results for the Allcal2 California fault model, *Seismol. Res. Lett.,* **83**(6), 994–1006.

Valensise, G. & Pantosti, D., 2001. The investigation of potential earthquake sources in peninsular Italy: a review, *J. Seismol.,* **5,** 287–306.

Valensise, G. Pantosti, D. & Basili, R., 2004. Seismology and tectonic setting of the 2002 Molise, Italy, earthquake, *Earthq. Spect.,* **20**(S1), 23–37.

van Stiphout, T. Zhuang, J. & Marsan, D., 2012. Seismicity declustering, Community Online Resource for Statistical Seismicity Analysis, doi:10.5078/corssa52382934. Available at: http://www.corssa.org.

Vannoli, P. Burrato, P. Fracassi, U. & Valensise, G., 2012. A fresh look at the seismotectonics of the Abruzzi (Central Apennines) following the 6 April 2009 L'Aquila earthquake (Mw 6.3), *Ital. J. Geosci.,* **131**(3), 309–329.

Vannoli, P. Burrato, P. & Valensise, G., 2015a. The seismotectonics of the Po Plain (northern Italy): tectonic diversity in a blind faulting domain. *Pure appl. Geophys.,* **172**(5), 1105–1142.

Vannoli, P. Vannucci, G. Bernardi, F. Palombo, B. & Ferrari, G., 2015b. The source of the 30 October 1930, Mw 5.8, Senigallia (Central Italy) earthquake: a convergent solution from instrumental, macroseismic and geological data, *Bull. seism. Soc. Am.,* **105**(3), 1548–1561.

Vere-Jones, D., 1969. A note on the statistical interpretation of Bath's Law, *Bull. seism. Soc. Am.,* **59**(4), 1535–1541.

Walters, R.J. *et al.*, 2018. Dual control of fault intersections on stop-start rupture in the 2016 Central Italy seismic sequence, *Earth planet. Sci. Lett.,* **500,** 1–14.

Ward, S.N., 2012. ALLCAL Earthquake Simulator. *Seismol. Res. Lett.,* **83**(6), 964–972.

Weichert, D.H., 1980. Estimation of the earthquake recurrence parameters for unequal observation periods for different magnitudes, *Bull. seism. Soc. Am.,* **70**(4), 1337–1346.

Yamashita, T., 1998. Simulation of seismicity due to fluid migration in a fault zone, *Geophys. J. Int.,* **132,** 674–686

Yikilmaz, M.B. Turcotte, D.L. Yakovlev, G. Rundle, J.B. & Kellog, L.H., 2011. Virtual California earthquake simulations: simple models and their application to an observed sequence of earthquakes, *Geophys. J. Int.,* **180,** 734–742.

APPENDIX A: PARAMETERS OF THE FAULT SYSTEMS ADOPTED IN THIS STUDY

Table A1. Geometric and kinematics parameters of the 54 FSs derived from DISS v. 3.2.1 (DISS Working Group 2018; http://diss.rm.ingv.it/diss/). Geometric coordinates refer to the upper left edge of the fault system. D: depth of the upper edge of the fault system from the sea level; S: strike; R: rake; L-t: length of the top of the fault system along its strike; L-b: length of the bottom of the fault system measured along its strike; W: fault system width measured along its dip; Slip-R: minimum and maximum slip-rate.

ID	Lat °N	Lon °E	D (km)	S (°)	Dip (°)	R (°)	L-t (km)	L-b (km)	W (km)	Slip-R (mm yr^{-1})	DISS source
S01	42.4098	13.0284	1.0	133	53	270	117.0	117.0	17.9	0.10–1.70	ITCS025
S02	43.8812	11.5185	0.5	298	33	270	33.1	33.1	13.8	0.10–1.00	ITCS037
S03	43.6447	11.7655	0.5	323	33	270	32.9	35.3	13.8	0.10–1.00	ITCS037
S04	43.5562	11.9977	0.5	292	33	270	17.8	15.3	13.8	0.10–1.00	ITCS037
S05	43.4140	12.1839	0.5	316	33	270	21.8	24.6	13.8	0.10–1.00	ITCS037
S06	42.6418	12.8171	0.5	329	33	270	100.0	102.1	13.8	0.10–1.00	ITCS037
S07	42.4776	13.0369	0.5	314	33	270	23.7	22.0	13.8	0.10–1.00	ITCS037
S08	42.5539	13.1559	2.0	134	50	270	73.0	73.0	15.0	0.10–1.00	ITCS013
S09	42.0877	13.8071	2.0	143	50	270	40.5	40.5	15.0	0.10–1.00	ITCS013
S10	43.6231	12.0966	1.0	133	45	270	20.5	20.5	5.7	0.10–1.00	ITCS041
S11	43.4140	12.4442	2.0	131	20	270	26.0	26.0	11.8	0.10–1.00	ITCS056
S12	43.2603	12.7436	2.5	148	45	270	80.0	82.2	16.2	0.10–1.00	ITCS028
S13	42.6443	13.2693	2.5	138	45	270	24.0	24.0	16.2	0.10–1.00	ITCS028
S14	42.4339	13.4536	1.0	134	53	270	64.0	64.0	16.0	0.10–1.00	ITCS040
S15	44.2056	11.5413	12.0	122	38	90	55.4	53.2	16.3	0.10–0.50	ITCS027
S16	43.9344	12.1325	12.0	133	38	90	64.5	66.2	16.3	0.10–0.50	ITCS027
S17	43.5428	12.7298	12.0	125	38	90	32.9	28.0	16.2	0.10–0.50	ITCS027
S18	43.3565	13.0711	12.0	153	38	90	54.9	57.3	16.2	0.10–0.50	ITCS027
S19	42.9130	13.3843	12.0	142	38	90	41.0	41.0	16.2	0.10–0.50	ITCS027
S20	42.2489	13.9977	8.0	137	25	90	53.0	53.0	21.0	0.10–0.50	ITCS078
S21	44.1928	12.3932	2.0	133	30	90	34.2	34.2	16.0	0.10–0.50*	ITCS039
S22	43.9799	12.7662	3.0	118	30	90	11.0	9.4	9.0	0.20–0.52	ITCS032
S23	43.9282	12.8926	3.0	134	30	90	15.0	16.7	9.0	0.20–0.52	ITCS032

Table A1. Continued

ID	Lat °N	Lon °E	D (km)	S (°)	Dip (°)	R (°)	L-t (km)	L-b (km)	W (km)	Slip-R (mm yr^{-1})	DISS source
S24	43.8340	13.0275	3.0	121	30	90	15.4	14.0	9.0	0.20–0.52	ITCS032
S25	43.7567	13.1987	3.0	137	30	90	15.5	16.6	9.0	0.20–0.52	ITCS032
S26	43.6497	13.3263	3.0	129	30	90	10.2	10.2	9.0	0.20–0.52	ITCS032
S27	43.4537	13.4637	3.5	141	43	90	10.9	10.9	13.9	0.15–0.40	ITCS020
S28	43.3530	13.5705	3.5	159	43	90	35.7	37.4	13.9	0.15–0.40	ITCS020
S29	43.0512	13.7277	3.5	150	43	90	21.0	21.0	13.9	0.15–0.40	ITCS020
S30	42.8560	13.8718	3.5	171	43	90	56.5	56.5	13.9	0.15–0.40	ITCS020
S31	42.3008	14.1942	3.0	131	30	90	29.0	29.0	10.0	0.10–0.50	ITCS079
S32	44.1634	12.6349	3.0	133	30	90	21.0	21.0	8.0	0.20–0.52	ITCS030
S33	44.0277	12.8780	2.5	101	38	90	10.5	9.2	6.5	0.20–0.52	ITCS043
S34	44.0048	13.0139	2.5	123	38	90	9.5	8.0	6.5	0.20–0.52	ITCS043
S35	43.9525	13.1160	2.5	146	38	90	24.0	24.0	6.5	0.20–0.52	ITCS043
S36	43.7503	13.2820	3.0	110	38	90	6.6	6.6	5.7	0.10–0.50*	ITCS008
S37	43.7251	13.3695	3.0	122	38	90	13.2	13.2	5.7	0.10–0.50*	ITCS008
S38	43.6535	13.5211	3.0	139	38	90	16.5	16.5	5.7	0.10–0.50*	ITCS008
S39	43.5274	13.6653	3.0	158	38	90	25.0	25.0	5.7	0.10–0.50*	ITCS008
S40	44.1187	13.0016	2.0	118	33	90	25.8	25.8	9.2	0.20–0.52	ITCS106
S41	43.9977	13.2817	2.0	120	33	90	26.2	21.8	9.2	0.20–0.52	ITCS106
S42	43.8646	13.5625	2.0	158	33	90	18.6	18.6	9.2	0.20–0.52	ITCS106
S43	43.7077	13.5960	1.5	136	33	90	19.5	17.0	9.2	0.49–0.91	ITCS031
S44	43.5768	13.7571	1.5	153	33	90	11.0	11.0	9.2	0.49–0.91	ITCS031
S45	43.4857	13.8661	1.5	347	48	90	12.5	12.5	8.8	0.37–0.54	ITCS107
S46	43.4213	13.9479	1.5	309	48	90	7.8	6.1	8.8	0.37–0.54	ITCS107
S47	43.4231	13.9390	2.1	173	45	90	14.8	15.4	6.2	0.15–0.20	ITCS156
S48	43.2905	13.9591	2.1	160	45	90	20.8	20.8	6.2	0.15–0.20	ITCS156
S49	43.1033	14.0513	2.1	177	45	90	9.2	9.2	6.2	0.15–0.20	ITCS156
S50	43.0077	14.1170	4.8	167	49	90	10.7	10.7	4.3	0.15–0.20	ITCS159
S51	42.9068	14.1470	4.8	183	49	90	4.9	4.9	4.3	0.15–0.20	ITCS159
S52	42.8565	14.1424	4.8	197	49	90	8.5	8.5	4.3	0.15–0.20	ITCS159
S53	42.5240	13.3558	11.0	92	80	200	82.0	82.0	9.0	0.10–0.50	ITCS075
S54	42.2432	13.8043	11.0	95	80	200	154.0	154.0	9.0	0.10–0.50	ITCS059

*Minimum and maximum slip rates commonly adopted in DISS for reverse faults, in place of those actually listed in DISS 3.2.1. For those sources, slip rates, stemming from Maesano *et al*. (2013, 2015) refer to time intervals much longer (2 Ma) than those adopted for adjacent areas (125 ka).

APPENDIX B: A NEW ALGORITHM FOR ANALYSIS OF MULTIPLE EVENTS

In the frame of the 'multiple events' concept applied to both real and synthetic catalogues, we have developed a clustering analysis algorithm for their systematic search and recognition.

The algorithm parses seismic catalogues in the form of lists of event records (time, hypocentre coordinates, magnitude) and operates, at its innermost level, systematic comparisons on time-ordered $E_1 \rightarrow E_2$ event couples (time-ordered means that event E_1 temporally precedes event E_2).

E_1, E_2 events are checked for the simultaneous satisfaction of some constitutive conditions in order to be flagged as 'linked'. Searched multiple events are 'chains' of linked $E_1 \rightarrow E_2$ couples.

The constitutive conditions of 'clustering' criteria are comparisons between defined threshold values and the following parameters:

1. Minimum magnitude for the first event of the sequence (hereafter named 'pivot' event).
2. Time difference between events ($t_{E_2} - t_{E_1}$).
3. Distance between hypocentres ($\vec{x}_{E_2} - \vec{x}_{E_1}$).
4. Magnitude difference with the pivot event (different threshold values are checked for positive and negative differences).

Threshold values for criteria 1 and 4 are arbitrarily chosen, while 2 and 3 are derived from event magnitude following the Gardner & Knopoff (1974) empirical rules. Being $t_{GK}(M)$ and $r_{GK}(M)$ the time and distance empirically related to event magnitude, condition 2 is:

$$(t_{E_2} - t_{E_1}) \leq t_{GK}(mag_{E_1})$$

while for condition 3 we have considered the possibility of choosing one of the following:

$$\left|\vec{x}_{E_2} - \vec{x}_{E_1}\right| \leq \begin{cases} r_{GK}(mag_{E_1}) & (1) \\ \max[r_{GK}(mag_{E_1}), r_{GK}(mag_{E_2})] & (2) \\ r_{GK}(mag_{E_1}) + r_{GK}(mag_{E_2}) & (3) \end{cases}$$

The multiplets search is a procedure that parses a catalogue in a cyclic sequence of three phases (ABC, ABC, ABC, . . .) that are repeated until the end of the catalogue is reached. Fig. B1 shows this cycle and explains for each of the three A,B,C panels the underlying concepts.

The (A), upper panel shows a portion of the catalogue 'magnitude–time' plot: here the process starts by looking for a pivot event, whose magnitude must exceed the criterion-1 threshold (the plot red horizontal line). From here (event 1 in Fig. B1), the algorithm checks for the simultaneous fulfillment of criteria 2, 3 and 4 on any following couple of events.

Since all criteria must be satisfied, phase A reduces computational cost, searching a subset of events (hereafter named 'pool') that begins from the pivot and ends when criterion 2 fails: in the (A) plot the blue rectangles drawn from the dot events are t_{GK} wide

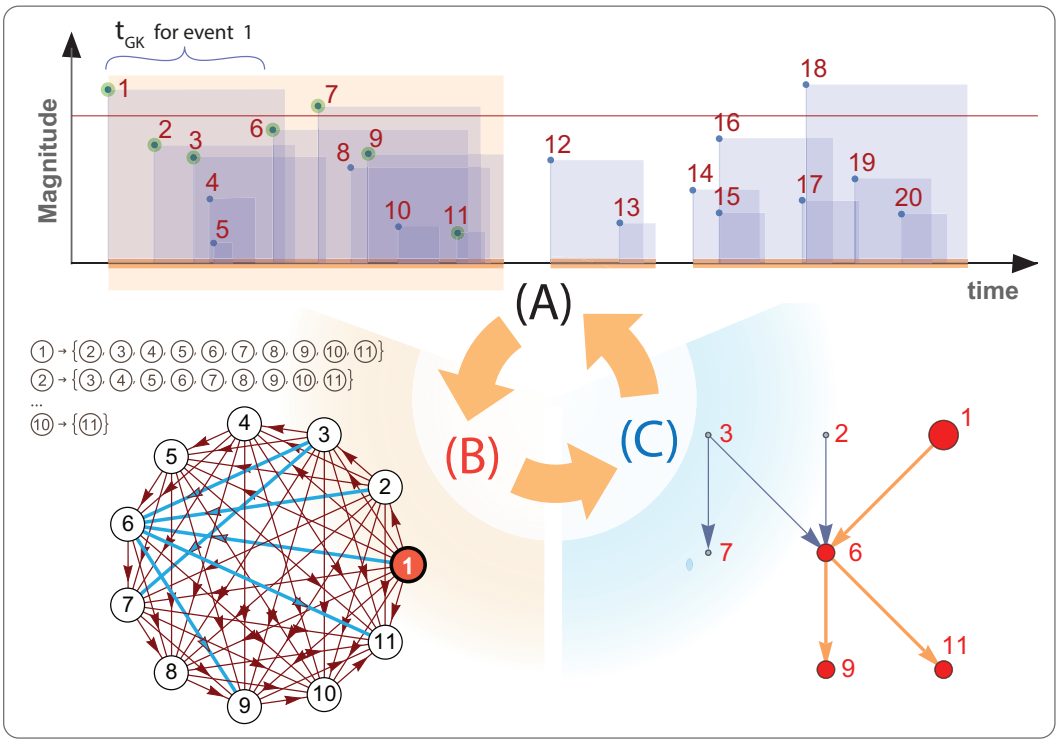

Figure B1. Multiplet search algorithm sequentially scans a seismic catalogue passing through A, B, and C steps, repeating the procedure until the catalogue ends. The top panel (A) is a time–magnitude scattergram of the searched catalogue. The red horizontal line is the threshold magnitude for pivots search. The figure example starts from event 1 as the first pivot. t_{GK} intervals (blue rectangles from dot events) form contiguous overlapping segments, shown as orange regions of time axis. The left-hand bottom panel (B) shows how the A-to-B comparison couples ensemble is generated and tested. A-to-B couples verifying 2, 3 and 4 criteria (blue arrows in left-bottom panel) generate the right-hand bottom panel (C) graph from which the searched multiplet can be found. The A-B-C procedure starts again finding the next pivot, according to the search removal conditions user issued. For instance, in the top panel, removed events are marked with green dots and next pivot will be event #18.

and their contiguous overlaps chain define the 'pools', indicated as orange intervals on time axis. In particular the pool related to pivot #1 in Fig. B1 contains events #1 to #11 and the $E_1 \rightarrow E_2$ couples to be checked are actually the panel (B) graph arrows (for n events there are $n(n–1)/2$ $E_1 \rightarrow E_2$ couples).

The $E_1 \rightarrow E_2$ couples that simultaneously satisfy the 2, 3 and 4 criteria are indicated as blue arrows in panel B graph. Panel (C) shows how these couples are then finally related to form the searched multiple event: they are a chain of events connected to the pivot and respecting comparison symmetry (the arrows directions). Since criteria 2 and 4 do contain asymmetrical relations (i.e. A and B order cannot be reversed), the chain is searched on an acyclic directed graph, respecting the edges orientations drawn from every $E_1 \rightarrow E_2$ event couples. If such a graph branch does exist (orange part of panel C graph) it is reported by the algorithm as a recognized multiple-event. A search for a new pivot (criterion 1) is thus issued and the whole procedure is repeated until the end of the catalogue.

In order to avoid the choice of a new pivot event that was already present in a reported multiple event, the algorithm has the possibility of removing from the search all the events present in the '2–3–4-connected' couples [i.e. the events present in the panel (C) graph] or, as a more stringent condition, the '2–3-connected-only' events. These conditions usually result in a notable limitation of the number of multiplets found. In Fig. B2, the '2–3–4-connected' events [all panel (C) acyclic graph nodes] are marked with green dots in panel (A) to show how the next pivot search will discard event #7 and find event #18.

Fig. B2 shows a concise flowchart of the whole procedure in which the (A), (B) and (C) portions are indicated with distinct background colours for reference. The procedure parses the catalogue through an indexes vector MP. The green blocks refer to operations on vector MP.

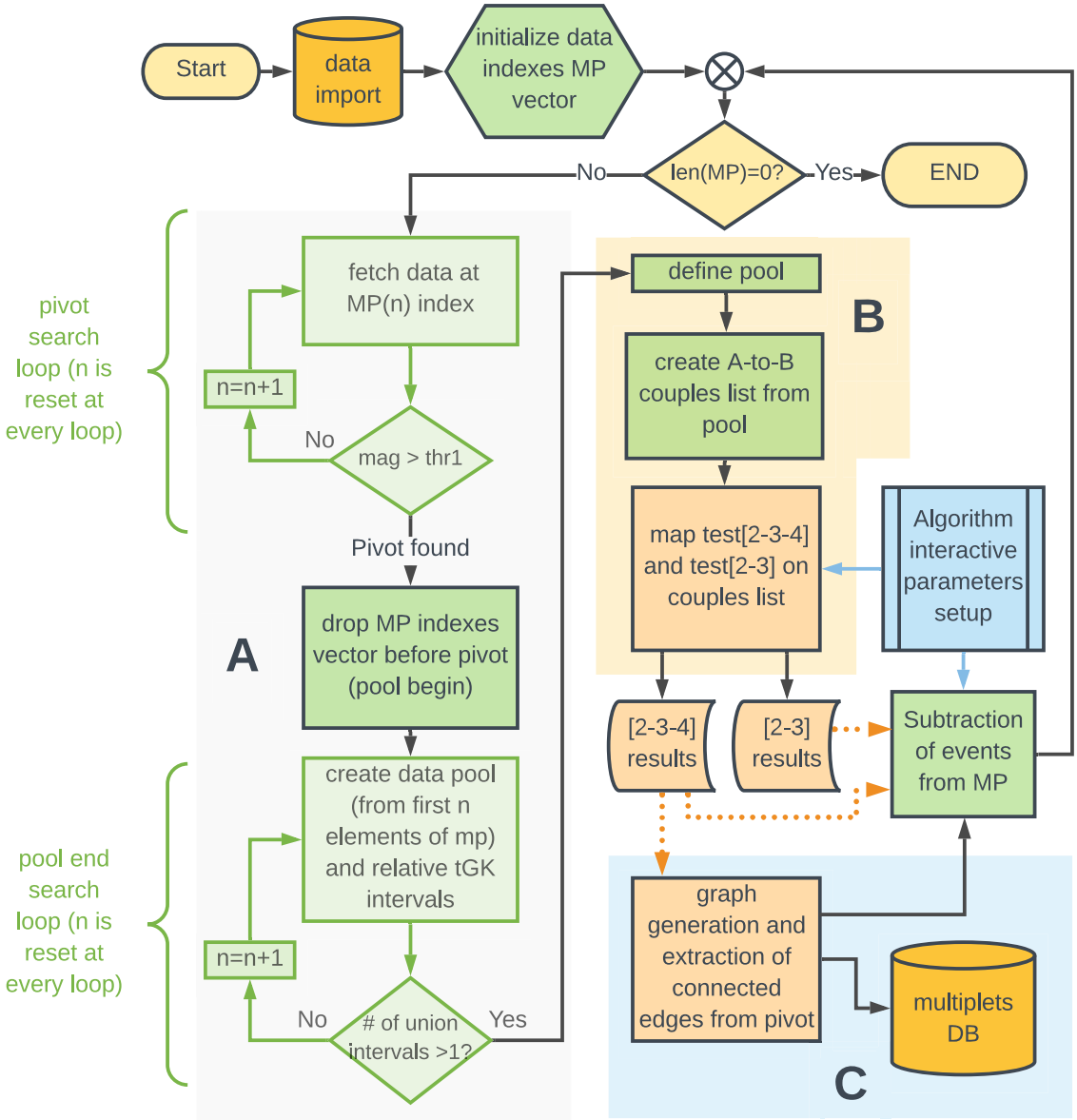

Figure B2. Flowchart of the multiple event search algorithm. A, B, C sections, for reference with Fig. 1, are indicated as coloured background regions. Blocks indicated with curly brackets are the pivot and pool bounds searching macros inside the main algorithm procedure: both make use of indirect indexing through a vector MP, initialized with all the integer indexes of the catalogue event list. All operations on MP components are indicated as green blocks. The algorithm keeps track of data parsing completion through data reference indexes in the MP vector, gradually deleting all used data indexes from MP. The procedure stops when MP is completely depleted.